Does the magnetic field suppress fragmentation in massive dense cores?

Palau, A.; Zhang, Q.; Girart, J.M.; Liu, J.; Rao, R.; Koch, P.M.; ... ; Ahmadi, A.

Draft version November 5, 2021
Preprint typeset using LaTeX style emulateapj v. 12/16/11

IN SEARCH FOR AN OBSERVATIONAL CORRELATION BETWEEN THE FRAGMENTATION LEVEL AND THE MAGNETIC FIELD PROPERTIES IN MASSIVE DENSE CORES

Aina Palau[1], Qizhou Zhang[2], Josep M. Girart[3,4], Junhao Liu[2,5,6], Ram Rao[2], Patrick M. Koch[7], Robert Estalella[8], Huei-Ru Vivien Chen[9], Hauyu Baobab Liu[7], Keping Qiu[5,6], Zhi-Yun Li[10], Luis A. Zapata[1], Sylvain Bontemps[11], Tao-Chung Ching[7], Hiroko Shinnaga[12], Paul T. P. Ho[7], Aida Ahmadi[13], Henrik Beuther[14]

Draft version November 5, 2021

ABSTRACT

Theoretical and numerical works indicate that a strong magnetic field should suppress fragmentation in dense cores. However, this has never been tested observationally in a relatively large sample of fragmenting massive dense cores. Here we use the polarization data obtained in the Submillimeter Array Legacy Survey of Zhang et al. (2014) to build a sample of 17 massive dense cores where both fragmentation and magnetic field properties are studied in a uniform way. We measured the fragmentation level, $N_{\rm mm}$, within the field of view common to all regions, of $\sim$ 0.15 pc, with a mass sensitivity of $\sim$ 0.5 $M_\odot$, and a spatial resolution of $\sim$ 1000 AU. In order to obtain the magnetic field strength using the Davis-Chandrasekhar-Fermi method, we estimated the dispersion of the polarization position angles, the velocity dispersion of the $H^{13}CO^+$ (4–3) gas, and the density of each core, all averaged within 0.15 pc. The magnetic field strength was also inferred using the Angular Dispersion Function method. Surprisingly, we found no apparent relation between the fragmentation level and the magnetic field strength, while a possible trend of $N_{\rm mm}$ with the average density of the parental core was found. In addition, the average masses of the fragments are comparable to the thermal Jeans mass. Therefore, our results suggest that thermal fragmentation and gravity dominate the fragmentation process in this sample. However, when only cores with similar densities are considered, there are hints of a possible anticorrelation between $N_{\rm mm}$ and the magnetic field strength.

Subject headings: stars: formation — radio continuum: ISM

1. INTRODUCTION

How stellar clusters form and what determines their number of objects and stellar densities is a long-standing question, intimately related to the fragmentation properties of molecular clouds. It is thought that a number of properties of molecular clouds could influence and determine how clouds fragment. First, their density and temperature structures determine the balance between thermal support and gravity required for pure thermal Jeans fragmentation (e. g., Myhill & Kaula 1992; Burkert et al. 1997; Girichidis et al. 2011). There are a number of additional properties however which could play a crucial role as well. The most important ones are the properties of turbulence (solenoidal/compressive and Mach number; e. g., Vázquez-Semadeni et al. 1996; Padoan & Nordlund 2002; Schmeja & Klessen 2004; Federrath et al. 2008; Girichidis et al. 2011; Keto et al. 2020), stellar feedback (e. g., Myers et al. 2013, Cunningham et al. 2018), initial angular momentum (e. g., Boss & Bodenheimer 1979; Boss 1999; Hennebelle et al. 2004; Machida et al. 2005; Forgan & Rice 2012; Chen et al. 2012a, 2019), and magnetic fields.

A number of theoretical and numerical studies suggest that magnetic fields could be a key ingredient in the fragmentation process of molecular clouds, because it is a form of support against gravitational contraction (e. g., Boss 2004; Vázquez-Semadeni et 2005, 2011; Ziegler 2005; Price & Bate 2007; Commerçon et al. 2011; Peters et al. 2011; Bailey & Basu 2012; Myers et al. 2013; Boss & Keiser 2013, 2014; Girichidis et al. 2018; Hennebelle & Inutsuka 2019). Therefore, it is expected that those cores with stronger magnetic fields should present a smaller degree of fragmentation, along with fragment masses larger than the pure thermal Jeans mass, compared to cores with weaker magnetic fields. This should hold at least for cores with similar densities and turbulence.

Massive dense cores are excellent targets to study the formation of stellar clusters. These are dense cores embedded within molecular clumps, with large masses ($\gtrsim$ 50 $M_\odot$) and typical sizes of 0.1–0.5 pc, which do not necessarily collapse into one star but can fragment into compact condensations

a.palau@irya.unam.mx
[1] Instituto de Radioastronomía y Astrofísica, Universidad Nacional Autónoma de México, P.O. Box 3-72, 58090, Morelia, Michoacán, Mexico
[2] Center for Astrophysics | Harvard & Smithsonian , 60 Garden Street, Cambridge, MA 02138, USA
[3] Institut de Ciències de l'Espai (CSIC-IEEC), Campus UAB, Carrer de Can Magrans S/N, E-08193 Cerdanyola del Vallès, Catalonia, Spain
[4] Institut d'Estudis Espacials de Catalunya, E-08030 Barcelona, Catalonia, Spain
[5] School of Astronomy and Space Science, Nanjing University, 163 Xianlin Avenue, Nanjing 210023, People's Republic of China
[6] Key Laboratory of Modern Astronomy and Astrophysics (Nanjing University), Ministry of Education, Nanjing 210023, People's Republic of China
[7] Institute of Astronomy and Astrophysics, Academia Sinica, No.1, Sec. 4, Roosevelt Rd, Taipei 10617, Taiwan
[8] Departament de Física Quántica i Astrofísica, Institut de Ciències del Cosmos, Universitat de Barcelona, (IEEC-UB) Martí i Franquès, 1, E-08028 Barcelona, Spain
[9] Institute of Astronomy and Department of Physics, National Tsing Hua University, Hsinchu 30013, Taiwan
[10] Astronomy Department, University of Virginia, Charlottesville, VA 22904, USA
[11] Université de Bordeaux, Laboratoire d'Astrophysique de Bordeaux, CNRS/INSU, UMR 5804, BP 89, 33271 Floirac Cedex, France
[12] Department of Physics and Astronomy, Graduate School of Science and Engineering, Kagoshima University, Amanogawa Galaxy Astronomy Research Center, 1-21-35 Korimoto, Kagoshima 890-0065, Japan
[13] Leiden Observatory, Leiden University, PO Box 9513, 2300 RA Leiden, The Netherlands
[14] Max Planck Institute for Astronomy, Königstuhl 17, 69117 Heidelberg, Germany

TABLE 1
PROPERTIES OF THE OBSERVATIONS USED TO ASSESS THE FRAGMENTATION LEVEL IN THE SAMPLE OF MASSIVE DENSE CORES AT 0.87 AND 1.3 MM

Source[a]	D (kpc)	L_{bol}[b] ($L_\odot$)	Rms[c] (mJy)	M_{min}[c] ($M_\odot$)	uv−range (kλ)	Spat. res.[d] (AU)	LAS[d] (AU)	Refs.[e]
1-W3IRS5	1.95	140000	2.4	0.31	22–210	1600	8050	1
2-W3H2O	1.95	36000	2.6*	1.22	55–585	682	3230	2,3
3-G192	1.52	2700	4.2	0.33	40–260	1070	3460	4,5
4-NGC 6334V	1.30	40000	7.0	0.42	25–210	1140	4730	4,6
5-NGC 6334A(IV)	1.30	1000	6.6	0.40	25–210	1200	4730	4
6-NGC 6334I	1.30	48000	12	0.72	25–210	1130	4730	4
7-NGC 6334In	1.30	1300	17	1.03	25–210	1190	4730	4
8-G34.4.0	1.57	2300	6.4	0.54	40–260	1110	3570	4
9-G34.4.1	1.57	1100	2.0	0.17	40–260	1160	3570	4
10-G35.2N	2.19	15000	2.3	0.38	40–260	1620	4980	4
11-IRAS 20126+4104	1.64	8900	0.7*	0.46	48–551	629	3120	7,8
12-CygX-N3(DR17)	1.40	200	1.1*	0.28	20–200	1400	6370	9,10
13-W75N(CygX-N30)	1.40	20000	2.6*	0.72	20–160	1650	6370	11
14-DR21OH(CygX-N44)	1.40	10000	4.7	0.33	40–260	1050	3150	4,12
15-CygX-N48(DR21OHS)	1.40	4400	2.2*	0.57	20–200	1400	6370	9,13
16-CygX-N53	1.40	300	1.9*	0.49	20–200	1400	6370	9,13
17-CygX-N63(DR22)	1.40	470	4.2*	1.08	20–200	1400	6370	9,10

[a] Complete names commonly used for each massive dense core. In the following tables and figures a short version of the name will be used.

[b] L_{bol} is calculated with the flux densities used to build the spectral energy distribution for the model described in Section 4.1.

[c] Rms at 870 μm (from SMA observations) for all sources, except for those marked with an asterisk, for which the rms corresponds to the image at $\sim$ 1.3 mm (Plateau de Bure and/or NOEMA observations). M_{min}, the mass sensitivity, is taken at 6 times the rms noise of each image (identification threshold) and assuming a dust temperature of 20 K.

[d] Spatial resolution taken from the synthesized beam of each image and the distance to the source. LAS stands for Largest Angular Scale, estimated using the smallest uv-distance given in column (6), and following equation A5 of Palau et al. (2010). This corresponds to the maximum spatial scale the interferometer was able to recover.

[e] References for the continuum emission used to assess the fragmentation level N_{mm} and for the polarization data used to study the polarization angle dispersion: (1) Chen et al., in preparation; (2) Ahmadi et al. (2018): this region is part of the CORE Large Project carried out with NOEMA (Beuther et al. 2018); (3) Chen et al. (2012b); (4) Zhang et al. (2014); (5) Liu et al. (2013); (6) Juárez et al. (2017); (7) Cesaroni et al. (2014); (8) Shinnaga et al. (in preparation); (9) Bontemps et al. (2010); (10) SMA archive; (11) Alves et al. (in preparation); (12) Girart et al. (2013); (13) Ching et al. (2017).

and form a small cluster of stars[15] (Williams et al. 2000; Bontemps et al. 2010; Motte et al. 2007). This makes massive dense cores excellent candidates to study forming clusters, which are usually associated with intermediate/high-mass stars. The fragmentation properties in samples of about $\sim$ 20 massive dense cores have been studied by a number of authors (e. g., Bontemps et al. 2010; Palau et al. 2014, 2015; Beuther et al. 2018; Fontani et al. 2018; Sanhueza et al. 2019; Svoboda et al. 2019). In these works, relations between the fragmentation level and density structure, turbulence and initial angular momentum were searched for, but none of these works studied if there is the expected relation between the fragmentation level and the magnetic field strength from an observational point of view.

Observational studies of fragmentation vs magnetic fields are very scarce. Most of the studies approaching this key question are based on a comparison of observations of dust continuum emission to the outputs of magneto-hydrodynamical simulations. For example, for the low-mass case, Maury et al. (2010) find that magneto-hydrodynamical models agree much better with their observations. And for the intermediate/high-mass case, Peretto et al. (2007) find difficulties matching the observed masses and number of fragments with the results of hydrodynamical simulations, suggesting that an extra support such as protostellar feedback or magnetic fields is at play. This is supported by the more recent works of Palau et al. (2013) and Fontani et al. (2016, 2018), where the number, mass and spatial distribution of the fragments of particular regions are consistent with simulations of fragmenting cores with different mass-to-flux ratios (Commerçon et al. 2011). However, the extreme fragmentation in the DR21OH core cannot be fully reproduced in these simulations because its measured mass-to-flux ratio is 20 times smaller than the one used in the simulations for the highly fragmenting cores (Girart et al. 2013).

Regarding studies reporting a direct measure of the magnetic field strength compared to fragmentation levels, Santos et al. (2016) present polarimetric data at optical and near-infrared wavelengths towards an infrared dark cloud with different fragmentation levels in two hubs (Busquet et al. 2016), and find no significant differences between the magnetic field at each hub at clump scales, while submillime-

[15] Strictly speaking, the entity which will contain the entire cluster should be the molecular clump (with sizes $\sim$ 1 pc), while probably the massive dense core will contain only the central or most embedded part of the stellar cluster (Zhang et al. 2009, 2015; Csengeri et al. 2011).

TABLE 2
FRAGMENTATION PROPERTIES OF THE MASSIVE DENSE CORES

Source	$N_{\rm mm}$[a]	Frag. type[b]	$\langle R_{\rm fragm}\rangle$[c] (AU)	$\sigma(R_{\rm fragm})$[c] (AU)	$\langle M_{\rm fragm}\rangle$[c] ($M_\odot$)	$\sigma(M_{\rm fragm})$[c] ($M_\odot$)	$M_{\rm Jeans}$[d] ($M_\odot$)	$M_{\rm crit}$[d] ($M_\odot$)
1-W3IRS5	4	cl	1490	70	0.14	0.1	17	12
2-W3H2O	8	cl	726	430	2.8	3.9	6.1	77
3-G192	1	no	1710	–	2.7	–	5.1	22
4-N6334V	5	cl	1310	460	1.1	1.3	3.7	44
5-N6334A	16	al	1270	370	1.3	1.1	2.4	29
6-N6334I	7	al	1070	620	3.8	6.8	4.3	160
7-N6334In	15	al	997	200	1.0	1.2	2.5	250
8-G34-0	2	no	1590	–	6.7	–	3.0	51
9-G34-1	10	al	1170	440	0.71	1.1	1.8	110
10-G35	13	al	1860	730	3.2	4.6	3.3	45
11-I20126	1	no	–	–	–	–	6.5	–
12-N3	6	al	1220	270	0.70	0.7	1.3	10
13-W75N	14	cl	1980	660	2.1	2.5	5.0	42
14-DR21OH	18	cl	1250	440	1.2	1.3	1.7	69
15-N48	6	cl	1430	300	0.98	0.6	1.4	21
16-N53	9	al	–	–	–	–	1.0	–
17-N63	1	no	2590	–	14	–	2.0	9.4

[a] $N_{\rm mm}$ is the fragmentation level, estimated counting the number of millimeter sources above a 6σ threshold, covering at least half a beam at 4σ, and closing at least one contour, within the common field of view for all the regions of 0.15 pc of diameter. For N63, $N_{\rm mm}$ was inferred from new Plateau de Bure observations in AB configuration (S. Bontemps, priv. communication).

[b] Fragmentation type according to Tang et al. (2019). 'cl' corresponds to 'clustered fragmentation'; 'al' corresponds to 'aligned fragmentation'; and 'no' corresponds to 'no fragmentation'.

[c] $\langle R_{\rm fragm}\rangle$ and $\langle M_{\rm fragm}\rangle$ correspond to the average radius and mass (at the 3σ level), respectively, of all fragments in a given massive dense core. $\sigma(R_{\rm fragm})$ and $\sigma(M_{\rm fragm})$ correspond to the standard deviation of the radius and mass of the fragments in each massive dense core. The mass of the fragments was calculated using the flux density within the 3σ contour, and considering the temperature corresponding to the temperature power-law derived in Section 4.1, using as distance the projected distance measured from the fragment to the peak of the single-dish submillimeter source. The opacity law used is the same as reported in Section E.

[d] $M_{\rm Jeans}$ corresponds to the Jeans mass calculated following equation (6) of Palau et al. (2015) and using the values of $n_{0.15\rm pc}$ and $T_{0.15\rm pc}$ listed in Table 3. $M_{\rm crit}$ is the magnetic critical mass (the Jeans mass analog in the magnetic support case) calculated following equation (16) of McKee & Ostriker (2007), for a diameter of 0.15 pc and the magnetic field strength $B_{\rm stdev}$ listed in Table 4.

ter polarization observations at core scales for the same two hubs reveal hints of a stronger magnetic field in the non-fragmenting case (Añez-López et al. 2020b). On the other hand, in the mini-starburst star-forming region W43, very recent Atacama Large Millimeter/submillimeter Array observations show similar magnetic field strengths for cores with different fragmentation levels (Cortés et al. 2019). Also in the G34.43+00.24 region the three cores studied by Tang et al. (2019) present different fragmentation levels, but they seem to result from an interplay between gravity, turbulence and magnetic field, with no clear evidence for a unique role of the magnetic field. In the first high resolution polarimetric imaging of a massive infrared dark cloud, Liu et al. (2020) find that magnetic fields play a role at the early stages of cluster formation. However, all the aforementioned observational works do not perform a uniform study in a relatively large sample of regions, but focus only on a single or a handful of regions at most. Galametz et al. (2018) study the submillimeter polarized emission in a sample of 12 low-mass Class 0 protostars, and find that the morphology of the magnetic field could be related to the rotational energy and the formation of single or multiple systems, with the magnetic field being aligned along the outflow direction for single sources. Thus, a uniform study of the fragmentation and magnetic field properties in a relatively large sample of massive dense cores is completely lacking and therefore imperative.

Here we used the submillimeter polarization data of the Submillimeter Array (SMA) Legacy Survey of Zhang et al. (2014), together with regions from the literature with similar observational properties to build a sample of 17 massive dense cores. In Section 2, we describe the sample and observations, in Section 3, we present the continuum, polarization and $H^{13}CO^+$ data, in Section 4 we analyze the polarization data, determine density profiles for all the sample, measure line widths, and perform the Angular Dispersion Function analysis to finally infer magnetic field strengths. In Section 5 a discussion of the results is presented and in Section 6 our main conclusions are given.

2. THE SAMPLE

In Table 1 we present the sample of 17 massive dense cores studied in this work. Among the 17 regions, the 0.87 mm polarization data of 11 were presented in the Submillimeter Array Legacy Survey of Zhang et al. (2014; see also Ching et al. 2017). The 0.87 mm polarization data of the remaining regions were taken from the literature or the SMA archive (see last column of Table 1). We thus refer to these works for the details of the polarization observations. In general, the typical 1σ rms noise in the Stokes Q and U images is of ~ 2 mJy beam^{-1}. It is worth noting that we took special care

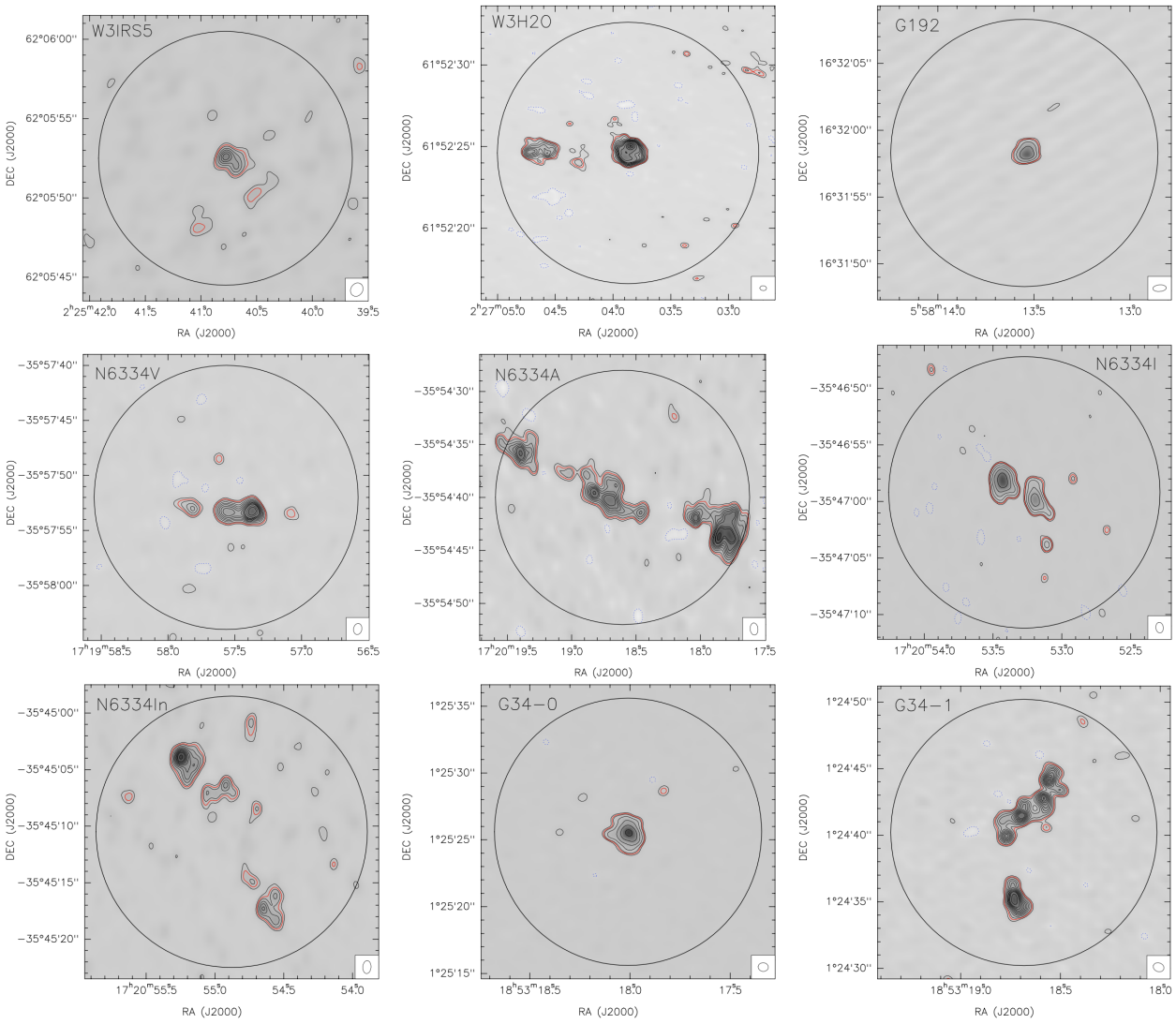

FIG. 1A.— 0.87 or 1.3 mm continuum high angular resolution maps. Contours for all regions are −4, 4, 8, 12, 16, 20, 24, 28, 36, 40, 50, 60, 70, 80, 100 and 120 times the rms noise, listed in Table 1, except for G192, N6334I, and G34-0, for which contours are −4, 4, 8, 16, 32, 64, and 128 times the rms noise. Synthesized beams are plotted in the bottom-right corner of each panel, and the black circle corresponds to a field of view of 0.15 pc diameter (the field of view common to all the regions, given their primary beams). In all panels the red contour corresponds to the identification level of 6σ.

to build a sample as uniform as possible. Thus, to avoid biases with distance, we restricted our sample to regions in the range 1.4–2.2 kpc, i. e., there is less than a factor of 2 in distance for the sources of our sample. Two of the regions were observed down to similar rms noises as the other regions, but no signal of polarized emission was detected: N53 from Ching et al. (2017), and I20126 from Shinnaga et al. (in preparation).

Regarding the continuum images used to assess the fragmentation level, Table 1 provides the properties of the images along with the references. For most of the regions we used the 0.87 mm continuum emission observed with the SMA using the extended configuration only from Zhang et al. (2014). Only those marked with an asterisk in Table 1 are observed with the Plateau de Bure(PdBI)/NOrthern Extended Millimeter Array (NOEMA) at 1.3 mm. In order to build a uniform sample, we specifically checked to ensure that the *uv*-coverage of both the SMA and PdBI/NOEMA are comparable (see column (6) of Table 1). This implied in some cases re-imaging using the visibilities only from the extended configuration. This will ensure not only a similar spatial resolution of $\sim$ 1000 AU for all the regions, but also that the largest angular scale filtered out by the interferometers is similar for all regions (see columns (7) and (8) of Table 1). Finally, special care was also taken regarding the sensitivity, which was required to be around $\sim$ 0.5 $M_{\odot}$ (at 6σ) or better. For this purpose, we self-calibrated some of the regions, with the final rms noises listed also in the table. We note that 6 of the regions included in the present sample (W3IRS5, I20126, DR21OH, N48, N53, and N63) overlap with the sample of Palau et al. (2014).

3. RESULTS

Figs. 1a and 1b present the resulting continuum images (with extended configuration only) used to assess the fragmentation level. The fragmentation level is estimated by counting the number of submillimeter sources above a 6σ threshold and within a region of 0.15 pc of diameter, which corresponds to the smallest field of view in our sample (given by the primary beam of the PdBI/NOEMA observations and

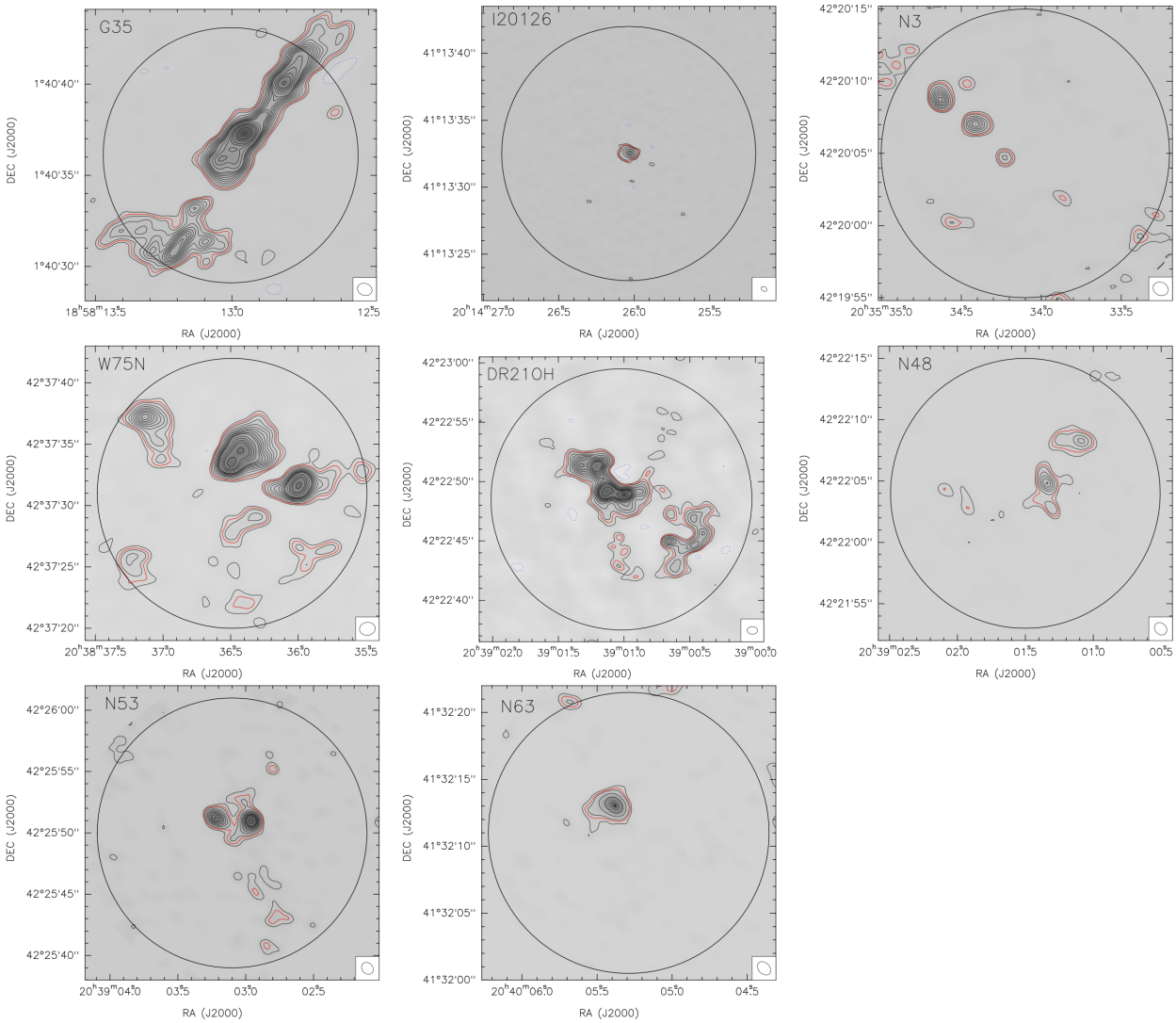

FIG. 1B.— 0.87 or 1.3 mm continuum high angular resolution maps. Contours for all regions are −4, 4, 8, 12, 16, 20, 24, 28, 36, 40, 50, 60, 70, 80, 100 and 120 times the rms noise, listed in Table 1, except for I20126 and N63 for which contours are −4, 4, 8, 16, 32, 64, and 128 times the rms noise. Synthesized beams are plotted in the bottom-right corner of each panel, and the black circle corresponds to a field of view of 0.15 pc diameter (the field of view common to all the regions, given their primary beams). In all panels the red contour corresponds to the identification level of 6σ.

the distance for each region). Table 2 lists the fragmentation level $N_{\rm mm}$ estimated for each region. As can be seen from the table, the measured fragmentation level ranges from no fragmentation at all (1 fragment for G192, I20126 and N63) to highly-fragmenting regions (with up to 18 fragments, such as DR21OH). A total number of 126 fragments were identified within the 17 massive dense cores. For each core, the mass and size (at the 3σ level) for each fragment was calculated (see details in Table 2), along with the average mass and size in each core, and their standard deviations. In addition, each massive dense core has been classified according a 'fragmentation type', following Tang et al. (2019): 'clustered fragmentation' corresponds to cores with fragments distributed more or less homogeneously within the core; 'aligned fragmentation' corresponds to cores with fragments predominantly aligned along a particular direction; 'no fragmentation' corresponds to cores with only 1 or 2 fragments. In order to ensure that the fragmentation level is not affected by biases with distance or sensitivity, in Fig. 13 of the Appendix we present $N_{\rm mm}$ vs spatial resolution and mass sensitivity, showing that there are no trends and thus the sample is well suited to compare the fragmentation properties between the different regions.

While the fragmentation level was assessed using only the SMA extended configuration, yielding typical synthesized beams below the arcsecond (~ 0.8) and filtering emission typically above $\sim 3''$, the polarized emission was obtained using all available SMA configurations, including compact and/or subcompact configurations, and therefore filtering out emission above 14″–30″ (Zhang et al. 2014). Thus, the polarized emission includes emission at much larger scales compared to the continuum emission used to study the fragmentation.

Figs. 2a and 2b present the magnetic field segments overplotted on the images of continuum emission used to assess the fragmentation level. From these figures it is clear that I20126 and N53 do not have enough detections to calculate their magnetic field strength, and hence will not be considered further for the analysis of the polarization data.

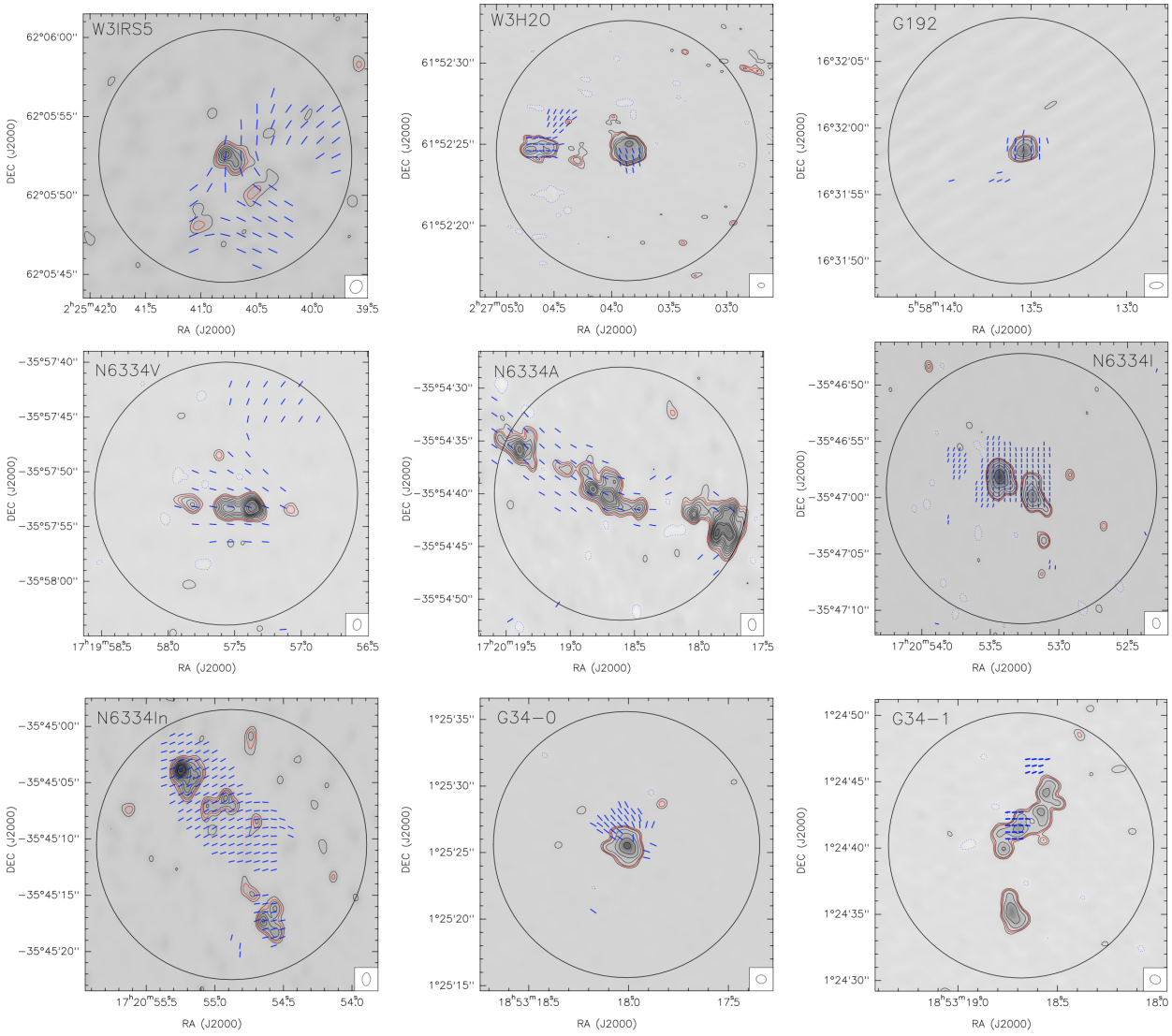

FIG. 2A.— 0.87 or 1.3 mm continuum high angular resolution maps with the magnetic field segments overplotted in blue. Contours for all regions are −4, 4, 8, 12, 16, 20, 24, 28, 36, 40, 50, 60, 70, 80, 100 and 120 times the rms noise, listed in Table 1, except for G192, N6334I, G34-0, and G34-1, for which contours are −4, 4, 8, 16, 32, 64, and 128 times the rms noise. For W3H2O contours are −4, 4, 8, 16, 24, 32, 64, 120 times the rms noise. Synthesized beams are plotted in the bottom-right corner of each panel, and the black circle corresponds to a field of view of 0.15 pc diameter (the field of view common to all the regions, given their primary beams).

In Figs. 14a and 14b of the Appendix we present the first-order moment of the $H^{13}CO^+$ (4–3) (346.998344 GHz) transition for each region. The observations of the $H^{13}CO^+$ (4–3) transition were carried out simultaneously with the submillimeter polarization data from the SMA, and the images presented in Figs. 14a and 14b correspond to images built using all available SMA configurations as for the polarized emission presented in Figs. 2a and 2b (therefore again including compact and/or subcompact configurations). Figs. 14a and 14b also show the outflow directions reported in the literature for each massive dense core.

4. ANALYSIS

4.1. *Determination of the density structure*

In order to estimate the density averaged within 0.15 pc of diameter (the field of view where the fragmentation level was assessed), we inferred the radial density profile of each massive dense core. To do this, we followed the same approach described in Palau et al. (2014), where a model was developed to simultaneously fit the radial intensity profiles at 450 and 850 μm SCUBA images (from the James Clerk Maxwell Telescope) from di Francesco et al. (2008)[16], along with the Spectral Energy Distribution (SED). The constraint imposed by the SED allows to break the degeneracy between temperature and density to the intensity of the source. The model assumes spherical symmetry, takes into account opacity effects, does not assume the Rayleigh-Jeans approximation and considers that the density and temperature decrease with radius following power-laws with indices p and q, respectively: $\rho = \rho_0(r/r_0)^{-p}$ and $T = T_0(r/r_0)^{-q}$, with ρ_0 and T_0 being the density and temperature values at a reference radius r_0 taken to be 1000 AU. Regarding the dust opacity law, it was

[16] For the cases of N3 and N63, the SCUBA data are not available and the IRAM 30m data at 1.2 mm from Motte et al. (2007) were used (Palau et al. 2014).

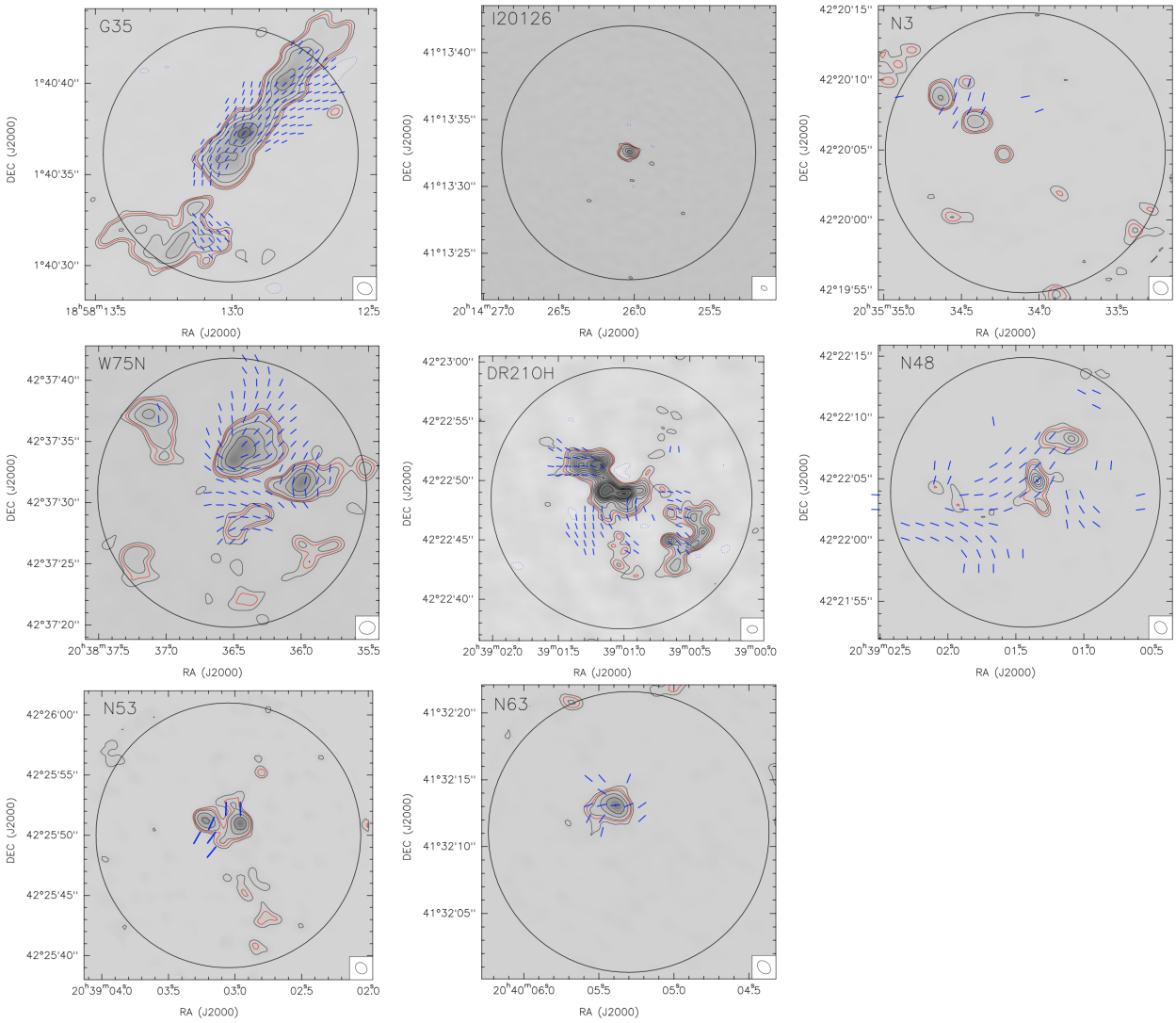

FIG. 2B.— 0.87 or 1.3 mm continuum high angular resolution maps with the magnetic field segments overplotted in blue. Contours for all regions are −4, 4, 8, 12, 16, 20, 24, 28, 36, 40, 50, 60, 70, 80, 100 and 120 times the rms noise, listed in Table 1, except for G35, I20126, W75N, N53 and N63 for which contours are −4, 4, 8, 16, 32, 64, and 128 times the rms noise. Synthesized beams are plotted in the bottom-right corner of each panel, and the black circle corresponds to a field of view of 0.15 pc diameter (the field of view common to all the regions, given their primary beams).

assumed to follow a power-law of frequency with index β, $\kappa = \kappa_0(\nu/\nu_0)^\beta$, where ν_0 is an arbitrary reference frequency. The value of $\kappa_0 = 0.008991$ cm^2 g^{-1} at $\nu_0 = 230$ GHz was adopted (Ossenkopf & Henning 1994). Given a dust cloud heated radiatively by a central luminous source, it has been shown that β and q are related according to $q = 2/(4+\beta)$ (Scoville & Kwan 1976; Adams 1991; Chandler et al. 1998). Thus, the final free parameters of the model are four: the dust emissivity index, β, the envelope temperature at the reference radius r_0, T_0, the envelope density at the reference radius r_0, ρ_0, and the density power-law index, p.

The fitting procedure was the same as the one described in Palau et al. (2014), with initial search ranges for the four parameters being $\beta = 1.5 \pm 1.5$, $T_0 = 300 \pm 300$ K, $\rho_0 = (1.0 \pm 1.0) \times 10^{-16}$ g cm^{-3}, and $p = 1.5 \pm 1.0$. The search range was reduced by a factor of 0.8 around the best-fit value found for each loop. In turn, each loop consisted of 2000 samples of the parameter space, and the final best-fit values were taken after 10 loops. Once the best-fit parameters were found, their uncertainties were estimated through the increase in χ^2. We refer to Palau et al. (2014) for further details of the model and the fitting procedure, and to Section C for additional details on the SED building for two particular regions of the sample. In Table 3 we list the best-fit values for the four free parameters of the model, along with the reduced χ^2, the temperature power-law index q, the mass within a region of 0.15 pc of diameter[17] and the density averaged within the same region. In Figs. 3a, 3b and 3c the observational data and the best-fit model for reach region are presented, and Fig. 5 shows a plot of the fragmentation level $N_{\rm mm}$ vs the density averaged within 0.15 pc. In this figure, the uncertainties associated with the density are obtained taking into account the uncertainty in the reference density ρ_0 and in the density power-law index p (Table 3). The figure reveals a

[17] The mass given in Table 3 is not the total mass of the core, but the mass only within a region of 0.15 pc of diameter. An estimate of the total mass of the core yields values typically about a factor of 4-10 larger than the mass within 0.15 pc of diameter.

TABLE 3
FITTED PARAMETERS OF THE DENSITY AND TEMPERATURE STRUCTURE OF THE MASSIVE DENSE CORES, INFERRED PROPERTIES AND VELOCITY DISPERSION

ID-Source	β^{a}	$T_0{}^{a}$ (K)	$\rho_0{}^{a}$ (g cm^{-3})	p^{a}	$\chi_r{}^{a}$	q^{b}	$M_{0.15pc}{}^{b}$ ($M_\odot$)	$n_{0.15pc}{}^{b}$ (10^5 cm^{-3})	$T_{0.15pc}{}^{b}$ (K)	$\Delta v_{0.15pc}{}^{c}$ (km s^{-1})
1-W3IRS5	1.04 ± 0.12	260 ± 30	$(2.4 \pm 0.3) \times 10^{-17}$	1.46 ± 0.04	0.602	0.40	22	2.23	118	3.20
2-W3H2O	1.30 ± 0.16	152 ± 16	$(1.5 \pm 0.2) \times 10^{-16}$	1.90 ± 0.05	0.532	0.38	59	5.84	82	9.67
3-G192	1.36 ± 0.23	66 ± 6	$(4.1 \pm 0.6) \times 10^{-17}$	2.13 ± 0.08	0.338	0.37	11	1.08	42	2.43
4-N6334V	2.19 ± 0.25	96 ± 11	$(1.3 \pm 0.3) \times 10^{-16}$	1.89 ± 0.08	0.334	0.32	51	5.12	62	4.87
5-N6334A	2.18 ± 0.15	78 ± 8	$(4.6 \pm 0.7) \times 10^{-17}$	1.42 ± 0.05	0.455	0.33	46	4.60	44	1.34
6-N6334I	2.55 ± 0.22	111 ± 12	$(2.3 \pm 0.4) \times 10^{-16}$	2.02 ± 0.05	0.461	0.31	73	7.30	80	2.31
7-N6334In	2.10 ± 0.19	98 ± 12	$(8.8 \pm 1.5) \times 10^{-17}$	1.46 ± 0.05	0.518	0.32	81	8.06	55	3.28
8-G34-0	1.96 ± 0.24	63 ± 6	$(2.0 \pm 0.4) \times 10^{-16}$	2.26 ± 0.09	0.483	0.34	44	4.36	46	2.54
9-G34-1	1.39 ± 0.23	63 ± 7	$(8.2 \pm 1.5) \times 10^{-17}$	1.76 ± 0.08	0.488	0.37	42	4.17	33	1.98
10-G35	1.86 ± 0.15	90 ± 7	$(4.4 \pm 0.6) \times 10^{-17}$	1.53 ± 0.03	0.463	0.34	36	3.57	46	5.34
11-I20126	1.82 ± 0.24	86 ± 9	$(8.4 \pm 1.6) \times 10^{-17}$	2.21 ± 0.11	0.607	0.34	20	1.95	59	–
12-N3[d]	1.69 ± 0.31	45 ± 4	$(4.0 \pm 0.5) \times 10^{-17}$	1.58 ± 0.04	0.648	0.35	29	2.92	23	2.22
13-W75N	2.04 ± 0.18	112 ± 12	$(1.4 \pm 0.2) \times 10^{-16}$	1.99 ± 0.05	0.729	0.33	48	4.82	67	4.70
14-DR21OH	1.60 ± 0.26	73 ± 7	$(3.1 \pm 0.6) \times 10^{-16}$	1.98 ± 0.08	0.808	0.36	105	10.5	42	4.66
15-N48	1.88 ± 0.18	58 ± 5	$(1.0 \pm 0.2) \times 10^{-16}$	1.71 ± 0.05	0.459	0.34	56	5.59	31	2.87
16-N53[d]	1.55 ± 0.22	45 ± 4	$(9.7 \pm 1.8) \times 10^{-17}$	1.76 ± 0.07	0.487	0.36	49	4.92	24	–
17-N63[d]	1.80 ± 0.33	45 ± 3	$(6.5 \pm 1.1) \times 10^{-17}$	2.03 ± 0.07	0.570	0.34	20	2.01	27	2.36
18-N7538S	1.74 ± 0.19	93 ± 10	$(1.3 \pm 0.2) \times 10^{-16}$	1.72 ± 0.05	0.304	0.35	72	7.12	49	–

[a] Free parameter fitted by the model: β is the dust emissivity index; T_0 and ρ_0 are the temperature and density at the reference radius, 1000 AU; p is the density power law index; χ_r is the reduced χ as defined in equation (6) of Palau et al. (2014).

[b] Parameters of the massive dense cores inferred from the modeled density and temperature structures. q is the temperature power-law index. $M_{0.15pc}$ is the mass inside a region of 0.15 pc of diameter computed according: $M_{0.15pc} = M(R = 0.075pc) = 4\pi\rho_0 r_0^p \frac{R^{3-p}}{3-p}$; $n_{0.15pc}$ and $T_{0.15pc}$ correspond to average density and temperature inside a region of 0.15 pc of diameter. $T_{0.15\,pc}$ was estimated as $T_R = \frac{\int_0^R T(r)\rho(r)r^2 dr}{\int_0^R \rho(r)r^2 dr}$, where $T(r)$ and $\rho(r)$ were calculated as power laws with temperature at the reference radius given in column (3), temperature power-law index given in column (7), density at reference radius given in column (4) and density power-law index given in column (5) of this table. The final expression is $T_R = \frac{T_0(3-p)}{3-p-q}\left(\frac{r}{r_0}\right)^{-q}$.

[c] $\Delta v_{0.15pc}$ is the line width obtained from fitting a Gaussian to the $H^{13}CO^+$ (4–3) spectrum averaged over a region of 0.15 pc of diameter.

[d] Sources for which only the radial intensity profile at 1.2 mm was fitted.

possible trend of N_{mm} with density.

4.2. *Determination of the velocity dispersion*

For each region of our sample, we extracted the $H^{13}CO^+$ (4–3) spectrum averaged over a region of 0.15 pc in diameter (the field of view where fragmentation was assessed), and fitted a Gaussian. For the case of N6334I there is absorption towards the two strongest continuum sources and some emission from 5 to 10 km s^{-1} (velocities given with respect to the local standard of rest), but these features are very compact. The main emission is found in the velocity range from -15 to 0 km s^{-1}, and shows hints of two possible velocity components. However, since we are interested in the average spectrum within the region of $\sim 20''$, and to be conservative, one single Gaussian to the emission from -15 to 0 km s^{-1} was fitted. The spectra and the corresponding fits are shown in Fig. 4, and the velocity dispersions are listed in Table 3. As can be seen from the figure, most spectra appear to be well fitted with only one Gaussian. In Fig. 5 a plot of the fragmentation level vs velocity dispersion is also presented (with the uncertainty in velocity dispersion taken from the Gaussian fit).

4.3. *Determination of the magnetic field strength: the Davis-Chandrasekhar-Fermi method*

Polarization observations of thermal dust emission at submillimeter wavelengths constitute a powerful tool to estimate the magnetic field strength onto the plane of the sky, B_{pos}. In order to estimate this, the Davis-Chandrasekhar-Fermi method (DCF, Davis 1951; Chandrasekhar & Fermi 1953) has been widely used. In this method, it is assumed that the turbulent kinetic energy and the magnetic energy are equal, and that the turbulent gas induces the observed dispersion in the polarization position angles (PA). Therefore higher PA dispersions correspond to weak magnetic fields such that the turbulent gas can drag the field lines. Following Chandrasekhar & Fermi (1953), the magnetic field strength can be estimated from the following relation, once the density, ρ, velocity dispersion along the line of sight, $\sigma_{vel,los}$, and PA dispersion, σ_{PA}, are known:

$$B_{pos} = A\ \sqrt{4\pi\rho}\ \frac{\sigma_{vel,los}}{\sigma_{PA}}, \qquad (1)$$

where A is a numerical correction factor adopted to be 0.5 (Ostriker et al. 2001). This numerical factor was derived for the cases where equation (1) is valid, mainly for PA dispersions $\lesssim 25°$. For larger dispersions, σ_{PA} should be replaced by $\tan(\sigma_{PA})$ (Falceta-Gonçalves et al. 2008). In the following subsections we present two different approaches to estimate

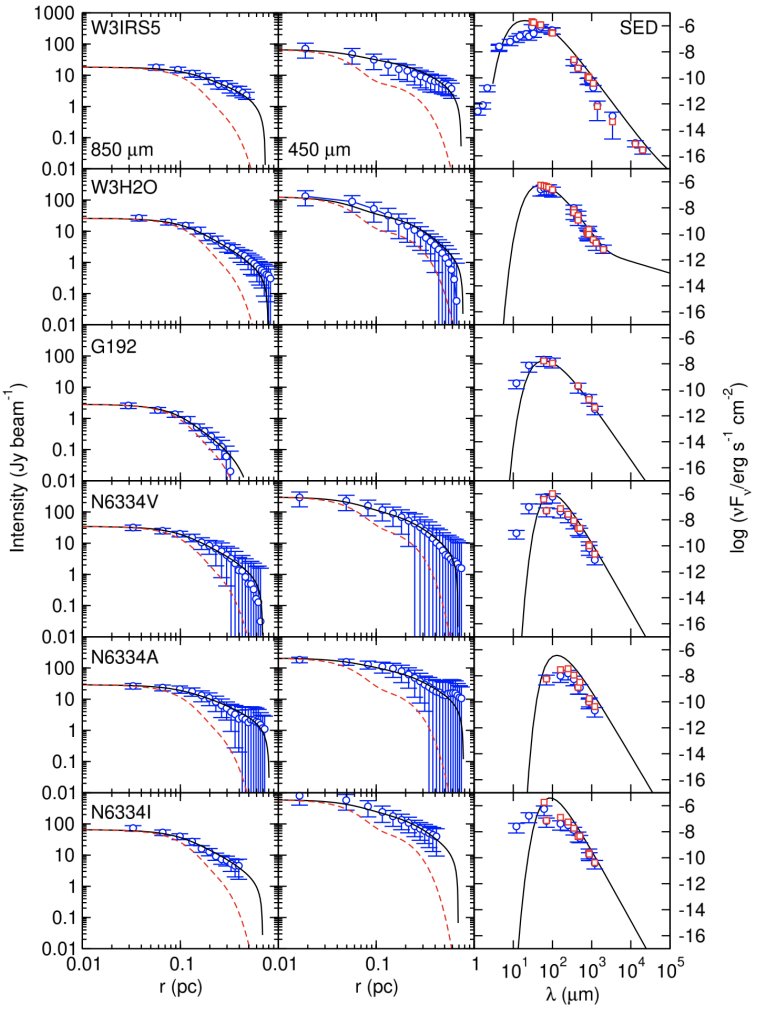

FIG. 3A.— Best fits for six regions of the sample (see Table 3 for the exact fitted parameters). Each row corresponds to one core, the left (middle) panel shows the radial intensity profile at 850 (450) μm, with the empty blue circles corresponding to the data, the black solid line corresponding to the model, and the dashed red line showing the beam profile; panels on the right show the SED, with blue empty circles indicating the observed fluxes, the black solid line showing the model for a fixed aperture, and the red squares corresponding to the model for the same aperture where each flux was measured.

the dispersion of the polarization PA.

4.3.1. *Polarization Position Angle Dispersion from standard deviation*

In order to estimate a dispersion in polarization PA, we extracted the PA values, Φ, from each PA image, for the same region where fragmentation was assessed (0.15 pc of diameter), and rejected those angles with an error larger than $\sim 10°$ ($11°$ for G34-1, and $15°$ for G192[18]), which corresponds to a S/N ratio smaller than 3 for the signal in polarization (Zhang et al. 2014). Three PA points per beam were extracted for each region.

A first approach to estimate the PA dispersion is based on the calculation of the standard deviation of the weighted mean. However, given the fact that the PA values have an error associated, it is desirable to subtract the contribution of the PA error to the PA dispersion. Thus, given a number N of PAs measured in a certain region, we have used the following expression:

$$\sigma_{\rm PA,stdev} = \sqrt{\frac{N\ \sum_{i=1}^{N} w_i\,(\Phi_i - \overline{\Phi}_w)^2}{(N-1)\sum_{i=1}^{N} w_i} - \frac{N}{\sum_{i=1}^{N} w_i}}, \qquad (2)$$

where $\overline{\Phi}_w = \frac{\sum_{i=1}^{N} w_i\,\Phi_i}{\sum_{i=1}^{N} w_i}$ is the weighted mean of PAs, and the second term within the square root corresponds to the contribution of the PA errors to the dispersion (equation A2 of Añez-López et al. 2020a). In these equations, w_i are the weights of each PA Φ_i, $w_i = 1/\delta\Phi_i^2$, with $\delta\Phi_i$ the PA error of each PA measurement. This final $\sigma_{\rm PA,stdev}$ can be considered as an intrinsic standard deviation, because the contribution from the PA errors has been removed.

The obtained values of $\sigma_{\rm PA,stdev}$ for each region are listed in Table 4. The PA dispersion ranges from 6 to 50°, and a plot of $N_{\rm mm}$ vs $\sigma_{\rm PA,stdev}$ is presented in Fig. 6. In this plot, the uncertainty in $\sigma_{\rm PA,stdev}$ was taken equal to the uncertainty of the weighted mean. If the magnetic field strength was directly

[18] Only for the case of G192 we included PA with errors $\sim 15°$ because an inspection of the PA values showed that there was two PA components, one around 20° and the other around 85°. The component around 20° is the one with large errors in the PA, but the different values of this component are very similar, making this component more significant (see Fig. 2a). 15° of PA error corresponds to a signal-to-noise ratio ~ 2.

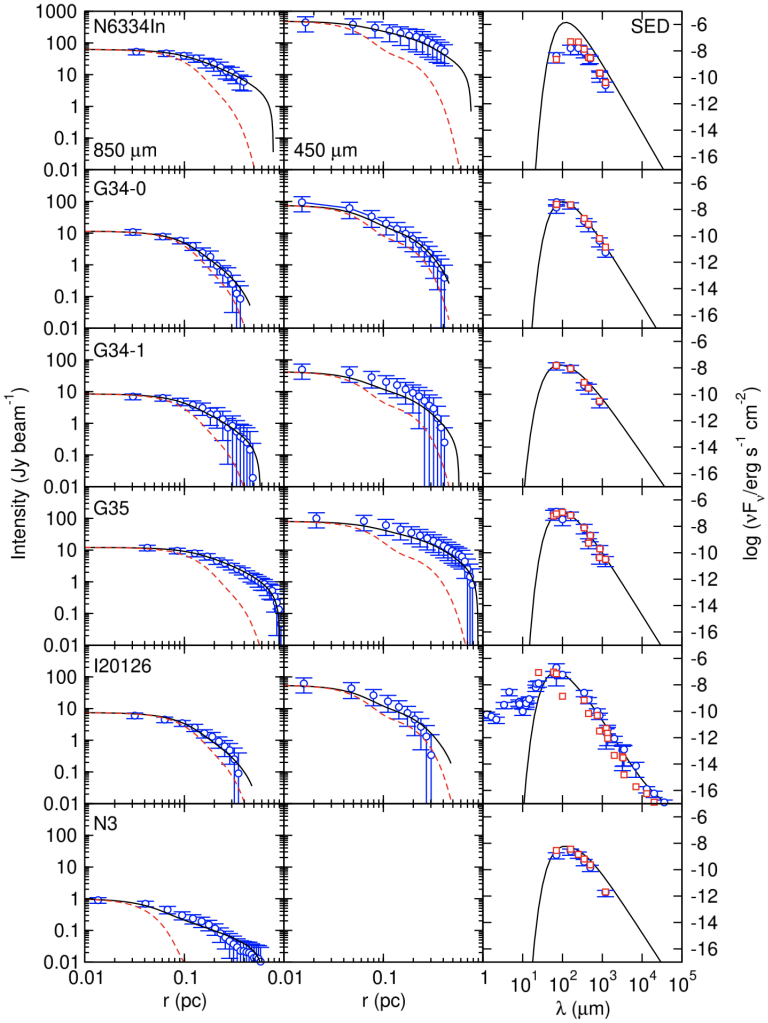

FIG. 3B.— Same as Fig. 3a.

related to the PA dispersion (as assumed in the DCF method) one would expect to find a positive trend in this figure, as a stronger magnetic field should yield a small PA dispersion and this in turn should prevent fragmentation. However, such a trend is not apparent from our figure.

4.3.2. *Polarization Position Angle Dispersion from multiple gaussian fitting*

In the previous Section, the PA dispersion was estimated by calculating the standard deviation of the PAs. However, the dispersion values calculated from equation (2) would systematically overestimate the dispersion in the cases where multiple components of the magnetic field are present. Thus, another approach to estimate the PA dispersion is to fit Gaussians to the histogram of PAs. The number of bins was determined using the 'auto' option of the 'histogram' function of Python, and the resulting histograms are presented in Fig. 7. For the cases of G192, N3 and N63, ∼ 4 points per beam were extracted from the PA image to allow a more robust fit of the histogram. In some cases, the histogram could be fitted with one single Gaussian component. In other cases, two (three) components were clearly separated in the PA histogram, and each component was fitted with a different Gaussian. However, there were cases clearly deviating from one single Gaussian but still with the two components merged so that it is ambiguous whether there are two (narrower) components or one (broader) component. In general, we considered separated PA components if the second peak of the tentative component is separated in y-axis by more than half of the peak of the strongest component while still being significant in number of points (around 5). This implied fitting two components for the ambiguous cases of N6334I, DR21OH, and N63[19], and three components for W75N.

The final PA dispersion was computed as the average from the different components, weighted by the area of each Gaussian. The results are presented in Fig. 7 and listed in Table 4. The uncertainty in $\sigma_{\rm PA,gauss}$ was taken equal to the uncertainty of the weighted mean as calculated in the previous section. Fig. 6 shows the fragmentation level against the PA dispersion using the multiple gaussian approach.

4.4. *Determination of the magnetic field strength: The Angular Dispersion Function method*

The previous approaches to estimate the PA dispersion could be introducing biases. First, the 'standard deviation' ap-

[19] For the case of N63, we also tried to fit 3 PA components. This implied a stronger magnetic field by less than a factor of two.

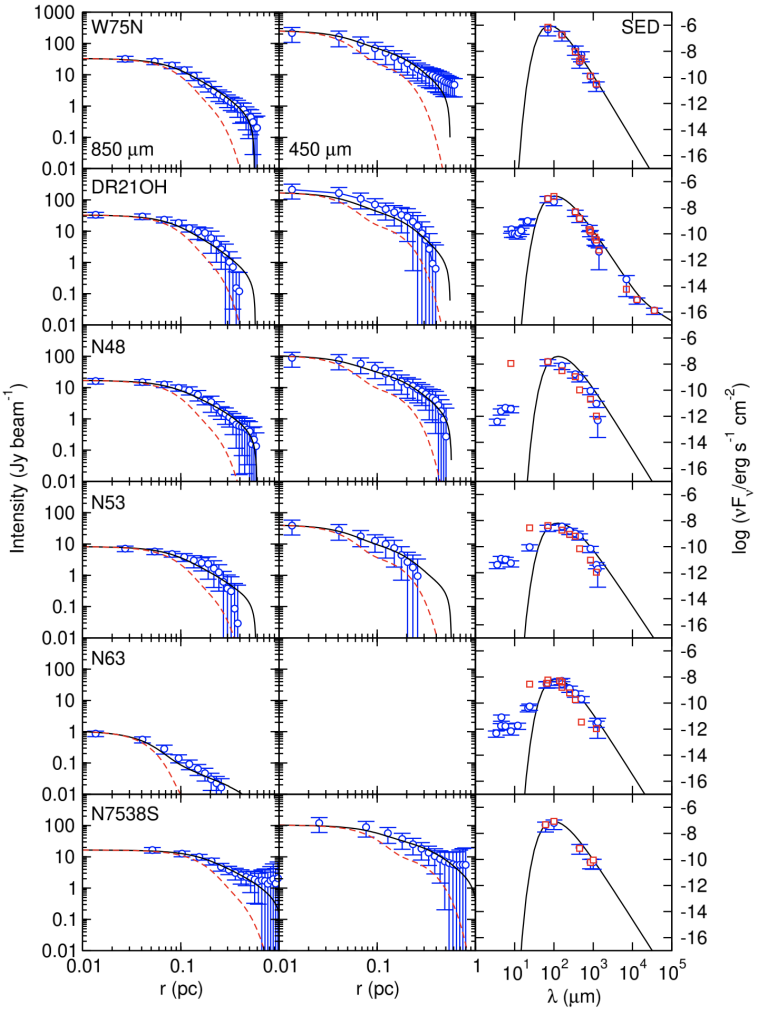

FIG. 3c.— Same as Fig. 3a.

proach could be overestimating the PA dispersion because it is ignoring the fact that there could be different magnetic field components within the same region. Second, the 'multiple gaussian' approach might be biased because of the decision of how many gaussian components should be used. Both the 'standard deviation' and the 'multiple gaussian' approaches might also be biased for broad PAs distributions where PAs separated about 180° actually correspond to the same direction. Fig. 7 shows that for 11 out the 15 regions studied here the different PA components are separated by less than 90° and should not be strongly affected by this problem. Only 4 regions present very broad distributions, W3H2O, W75N, N48, and N63, being W3H2O the most striking case (see also Table 4).

Another method to estimate $\sigma_{\rm PA}$ in equation (1) was first introduced by Houde et al. (2009), the so-called Angular Dispersion Function (ADF) method. This method does not suffer from the aforementioned biases, and takes into account the smoothing effect due to finite resolutions and the integration along the line of sight. In addition, it separates the contribution of large scale magnetic fields to angle dispersions because it assumes that there are two statistically independent components of the magnetic field. One component is related to the large-scale, ordered, magnetic field, B_0, and the other component corresponds to a perturbed or turbulent magnetic field, $B_{\rm t}$. With this assumption, Houde et al. (2009) applied ADF to study the change of polarization PA differences with distance, and related the output of this statistical analysis to the ratio of $B_{\rm t}$ energy to B_0 energy, $b \equiv \langle B_{\rm t}^2\rangle/\langle B_0^2\rangle$, which corresponds to $\sigma^2_{\rm PA}$ and can thus be used in equation (1). We refer the reader to Houde et al. (2009) for further details on this approach. In short, the ADF can be calculated as follows:

$$1 - \langle\cos[\Delta\Phi(l)]\rangle \simeq \frac{b}{N}\left(1 - e^{-l^2/(2\delta^2+4W^2)}\right) + a'_2\, l^2, \qquad (3)$$

where l is the length scale, δ is the magnetic field turbulent correlation length, W is the 'beam radius' ($W = FWHM/\sqrt{8\ln 2}$, with FWHM being the full width at half-maximum of the beam), a'_2 is the coefficient of the uniform parabolic approximation, and N is:

$$N \equiv \Delta'\,(\delta^2 + 2W^2)/(\sqrt{2\pi}\delta^3), \qquad (4)$$

with Δ' being the effective thickness of the cloud, expected to be slightly smaller than the cloud thickness. Here we assume that Δ' is equal to the core's effective thickness, taken as the diameter of the dense core in the plane of the sky as

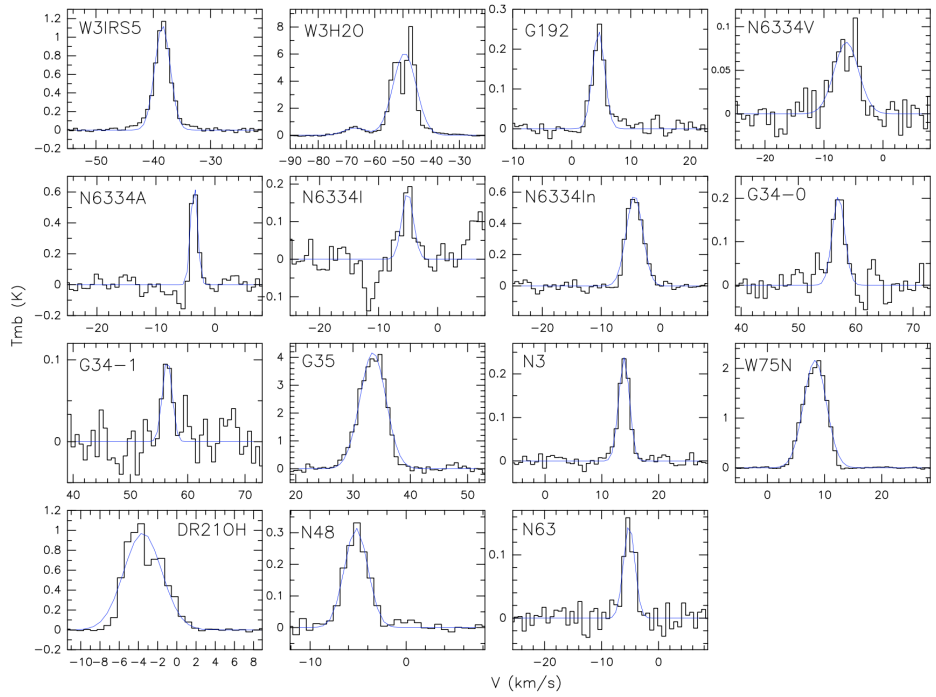

FIG. 4.— $H^{13}CO^+$ (4–3) spectra (black) with the gaussian fits (blue curves) performed to estimate the velocity dispersion in each region.

measured with the SMA (Koch et al. 2010). By fitting equation (3) to the observational data the values for the three free parameters, b/N, δ and a'_2, are obtained.

The ADF method can be applied for those regions with a very large number of detections of polarization PA so that the fitting of the ADF curve with three free parameters is robust. For our sample, we applied this approach only to 10 regions, which are those with more than 45 PA detections. Table 4 lists the three fitted parameters, δ, b/N, and a'_2, along with the adopted value for Δ' (estimated from the SMA continuum images combining all available configurations), and the corresponding values for N, $\langle B_t^2\rangle/\langle B_0^2\rangle$ and $\langle B_0^2\rangle^{1/2}$. Fig. 6 presents a plot of N_{mm} vs $\langle B_t^2\rangle/\langle B_0^2\rangle$. In this plot, a typical uncertainty of 0.05–0.1 has been adopted for the free parameter b/N controling $\langle B_t^2\rangle/\langle B_0^2\rangle$.

4.5. *A comparison between the DCF and ADF methods*

As mentioned above, the ADF method should be more robust than the 'standard deviation' and the 'multiple gaussian' approaches because it does not suffer from the aforementioned biases (although it also has large uncertainties associated, as shown by Liu et al. 2019), but unfortunately it could be applied only to 10 regions of our sample, while the other two approaches could be applied to 15 regions. If $\sigma_{PA,stdev}$ or $\sigma_{PA,gauss}$ were shown to correlate to $(\langle B_t^2\rangle/\langle B_0^2\rangle)^{1/2}$, this would suggest that such a determination of σ_{PA} is a reasonable approach. In Fig. 9 we present plots of $(\langle B_t^2\rangle/\langle B_0^2\rangle)^{1/2}$ vs $\tan(\sigma_{PA,stdev})$ and $\tan(\sigma_{PA,gauss})$ (see next paragraph regarding the use of $\tan(\sigma_{PA})$ instead of σ_{PA}), as well as $\sigma_{PA,stdev}$ vs $\sigma_{PA,gauss}$. The figure shows a tighter correlation between $(\langle B_t^2\rangle/\langle B_0^2\rangle)^{1/2}$ and $\tan(\sigma_{PA,stdev})$, with a correlation coefficient of 0.74 against 0.60 for the other two cases, suggesting that the determination of $\sigma_{PA,stdev}$ is a reasonable good approach to the real σ_{PA}. In the following, we will consider the value of $\sigma_{PA,stdev}$ as the reference value for σ_{PA}.

In Sections 4.3.1, 4.3.2, and 4.4, σ_{PA} was estimated using three different approaches. We then calculated the magnetic field strength following equation (1) and using the density and line width inferred in Sections 4.1 and 4.2, with all quantities averaged within 0.15 pc of diameter. We would like to emphasize that, while the fragmentation level is measured in SMA images obtained using only the extended configuration, thus filtering out typically angular scales larger than $\sim 3''$ (Table 1), the polarized and $H^{13}CO^+$ emissions are obtained from images including subcompact and/or compact SMA configurations, thus filtering out much larger scales, of $14''$–$30''$. The density is obtained from the modeling of the radial intensity profiles and SEDs obtained from single-dish data with angular resolutions $\gtrsim 11''$. Thus, the magnetic field strength is calculated using data sensitive to the core scale, and averaged within this same scale (of 0.15 pc of diameter).

For the 'standard deviation' and 'multiple gaussian' approaches, the correction introduced by Falceta-Gonçalves et al. (2008) was applied. This correction consists of using $\tan(\sigma_{PA})$ instead of σ_{PA} in equation (1), to finally compute the magnetic field strength, B_{stdev} and B_{gauss} (see Table 4). The uncertainty associated with the magnetic field strength was calculated by propagating the errors associated with the density, velocity dispersion and polarization PA dispersion, and a consistency check was performed by plotting B_{stdev} vs $n_{0.15pc}$ in Fig. 15 of the Appendix. The figure shows that there is a relation between these two quantities, as expected from equation (1). The results are reported in Table 4, and we plotted the fragmentation level N_{mm} vs B_{pos} in Fig. 10. We also calculated the ratio of the observed mass-to-flux over the critical mass-to-flux (Table 4), by following equation (1) of Crutcher et al. (2004). The figure shows that there is no apparent relation between N_{mm} and B_{pos}, or N_{mm} and the mass-to-flux ratio, for any of the approaches used here.

5. DISCUSSION

TABLE 4
MAGNETIC FIELD STRENGTHS DERIVED USING DIFFERENT APPROACHES

Source	$\sigma_{\rm PA,stdev}$[a] (°)	$B_{\rm stdev}$[a] (mG)	$\mu_{\rm stdev}$[a]	$\sigma_{\rm PA,gauss}$[b] (°)	$B_{\rm gauss}$[b] (mG)	$\mu_{\rm gauss}$[b]	δ[c] (mpc)	$\frac{b}{N}$[c]	a_2'[c] ($\rm pc^{-2}$)	Δ'[c] (mpc)	N[c]	$\frac{\langle B_{\rm t}^2\rangle}{\langle B_0^2\rangle}$[c]	$\langle B_0^2\rangle^{\frac{1}{2}}$[c] (mG)	$B_{\rm lit}$[d] (mG)	Refs.[d]
1-W3IRS5	50	0.2	1.9	23	0.6	0.6	32	1.1	−80	85	1.3	1.40	0.7	–	–
2-W3H2O	41	1.4	0.7	9.1	7.6	0.1	12	0.5	40	47	2.3	1.21	3.7	4.6	5
3-G192	18	0.4	0.4	8.0	0.9	0.2	–	–	–	–	–	–	–	–	–
4-N6334V	35	0.8	1.1	12	2.7	0.3	30	0.7	0	57	1.0	0.68	2.3	0.7	2
5-N6334A	16	0.5	1.5	6.8	1.2	0.6	20	0.1	25	63	2.4	0.34	0.9	–	–
6-N6334I	6.5	2.8	0.4	7.8	2.4	0.5	46	0.5	−70	50	0.4	0.23	2.3	2.8	6
7-N6334In	6.0	4.6	0.3	7.4	3.7	0.4	29	0.1	−1	50	0.8	0.08	5.9	3.2	6
8-G34-0	17	0.9	0.8	18	0.9	0.9	–	–	–	–	–	–	–	0.5	7
9-G34-1	6.0	2.0	0.4	6.2	1.9	0.4	–	–	–	–	–	–	–	1.1	7
10-G35	33	0.8	0.8	23	1.3	0.5	25	0.2	45	96	1.8	0.35	3.0	1.4	11
11-I20126	–	–	–	–	–	–	–	–	–	–	–	–	–	1.8	8
12-N3	47	0.2	2.8	8.6	1.3	0.4	–	–	–	–	–	–	–	0.3	9
13-W75N	35	0.8	1.1	24	1.3	0.6	12	0.5	−17	81	5.4	2.70	1.1	–	–
14-DR21OH	32	1.2	1.5	22	2.0	0.9	15	0.6	−70	68	2.0	1.28	2.3	1.8	3,10
15-N48	43	0.4	2.7	19	1.1	0.9	12	0.5	−16	101	7.2	3.78	0.6	0.5	4
16-N53	–	–	–	–	–	–	–	–	–	–	–	–	–	0.8	9
17-N63	46	0.2	2.1	25	0.4	0.9	–	–	–	–	–	–	–	–	–
18-N7538S														–	–

[a] $\sigma_{\rm PA,stdev}$ corresponds to the PA dispersion calculated within a region of 0.15 pc of diameter and using the standard deviation as described in Section 4.3.1. $B_{\rm stdev}$ is calculated using the DCF method and $\sigma_{\rm PA,stdev}$ (column 2 of this table), $n_{0.15\rm pc}$, and $\Delta v_{0.15\rm pc}$ of Table 3. $\mu_{\rm stdev}$ is the ratio of observed over critical mass-to-flux ratio, calculated following equation (1) of Crutcher et al. (2004): $\mu \equiv \frac{(M/\Phi)_{\rm obs}}{(M/\Phi)_{\rm crit}} = 7.6\times10^{-21}\frac{N_{\rm H_2}}{B_{\rm total}}$, where $N_{\rm H_2}$ is the gas column density in $\rm cm^{-2}$ obtained from Table 3 and considering a diameter of 0.15 pc, and $B_{\rm total}$ is the total magnetic field in μG, estimated from columns (3) and (6) and applying a factor of $4/\pi$ as a correction for the statistical mean value.

[b] $\sigma_{\rm PA,gauss}$ corresponds to the PA dispersion calculated within a region of 0.15 pc of diameter and fitting multiple gaussians as described in Section 4.3.2. $B_{\rm gauss}$ is calculated using the DCF method and $\sigma_{\rm PA,gauss}$ (column 5 of this table), $n_{0.15\rm pc}$, and $\Delta v_{0.15\rm pc}$ of Table 3. $\mu_{\rm gauss}$ is the ratio of observed over critical mass-to-flux ratio, calculated as in previous table note.

[c] δ, b/N, and a_2' are the three free parameters of the ADF method. δ is the magnetic field turbulent correlation length, b/N is the value of the correlated component at the origin, and a_2' is the coefficient of the uniform parabolic approximation. Δ' is the effective thickness of the cloud, estimated from the size of the SMA continuum emission obtained using all configurations. N is the number of turbulent cells along the line of sight. $\langle B_{\rm t}^2\rangle/\langle B_0^2\rangle$ is the ratio of the perturbed magnetic field energy vs the ordered magnetic field energy. $\langle B_0^2\rangle^{\frac{1}{2}}$ is the ordered magnetic field strength. See Section 4.4 for further details on each parameter.

[d] (2) Juárez et al. (2017), ADF; (3) Girart et al. (2013), ADF; (4) Ching et al. (2017), ADF; (5) Chen et al. (2012b), DCF; (6) Li et al. (2015): force equilibrium between gravity and magnetic tension and magnetic pressure; (7) Tang et al. (2019), ADF for single-dish; (8) Edris et al. (2005), Zeeman effect of OH masers; (9) Hezareh et al. (2013), ion-neutral; (10) Hezareh et al. (2010), ion-neutral; (11) Qiu et al. (2013), ADF.

5.1. *Uncertainties in the determination of the magnetic field strength*

In previous sections we estimated the magnetic field strength in the plane of sky following the DCF and ADF methods, and searched for a possible trend of this quantity with the fragmentation level. We found no clear trend between these two quantities. Before discussing the physical implications of this result, we should consider how robust our determination of the magnetic field strength is. In Fig. 10 we plotted the magnetic field strength with the corresponding uncertainties after taking into account the uncertainties in the density (Section 4.1), velocity dispersion (Section 4.2) and polarization PA dispersion (Section 4.3). Only three regions with large relative errors in the PA dispersions (N6334I, N6334In and G34-1) present large uncertainties, of $\sim$ 2 mG, while the other regions present smaller uncertainties in the range 0.1–0.4 mG.

Regarding the estimate of the density, an additional uncertainty could come from the different spatial filtering of single-dishes (used to assess density) vs interferometers (used to assess velocity and PA dispersions). To assess how much the different spatial filtering of each telescope could affect our determination of the magnetic field strength, the average density was estimated using the SMA continuum flux densities, including all the configurations available as for the case of the polarization and $\rm H^{13}CO^+$ data. For each region, we estimated the total mass recovered by the SMA (see Appendix) and found that the amount of mass filtered out by the SMA is on average only $\sim$ 25% of the mass inferred from the modeling of the single-dish data presented in Section 4.1. In Fig. 16 of the Appendix, we present a plot of the SMA average density vs single-dish average density, showing a relation close to 1-1, with the SMA densities only slightly below the single-dish densities. Therefore, the slightly different spatial filtering between the single-dish and the SMA is not heavily affecting

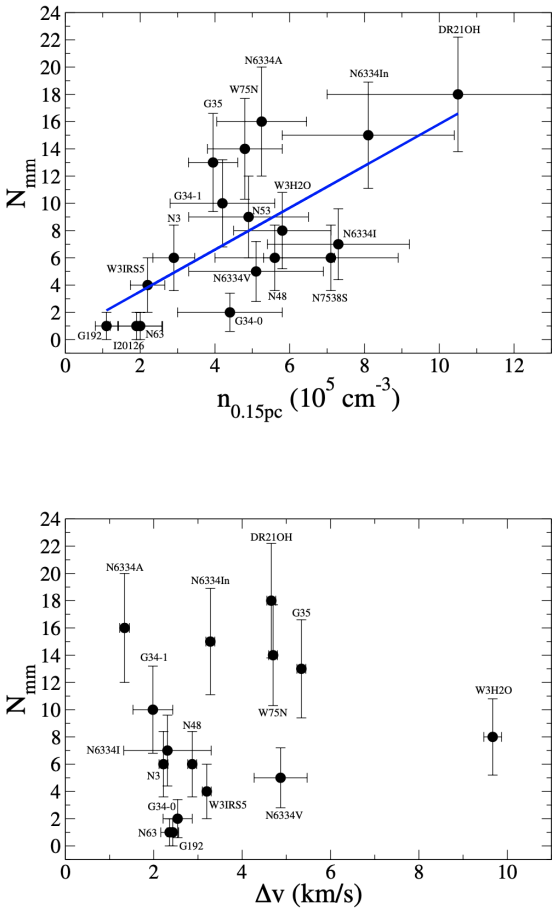

FIG. 5.— Top: Fragmentation level vs density averaged within the same field of view where fragmentation, line width and PA dispersion were assessed (0.15 pc of diameter). Bottom: Fragmentation level vs line width of the $H^{13}CO^+$ (4–3).

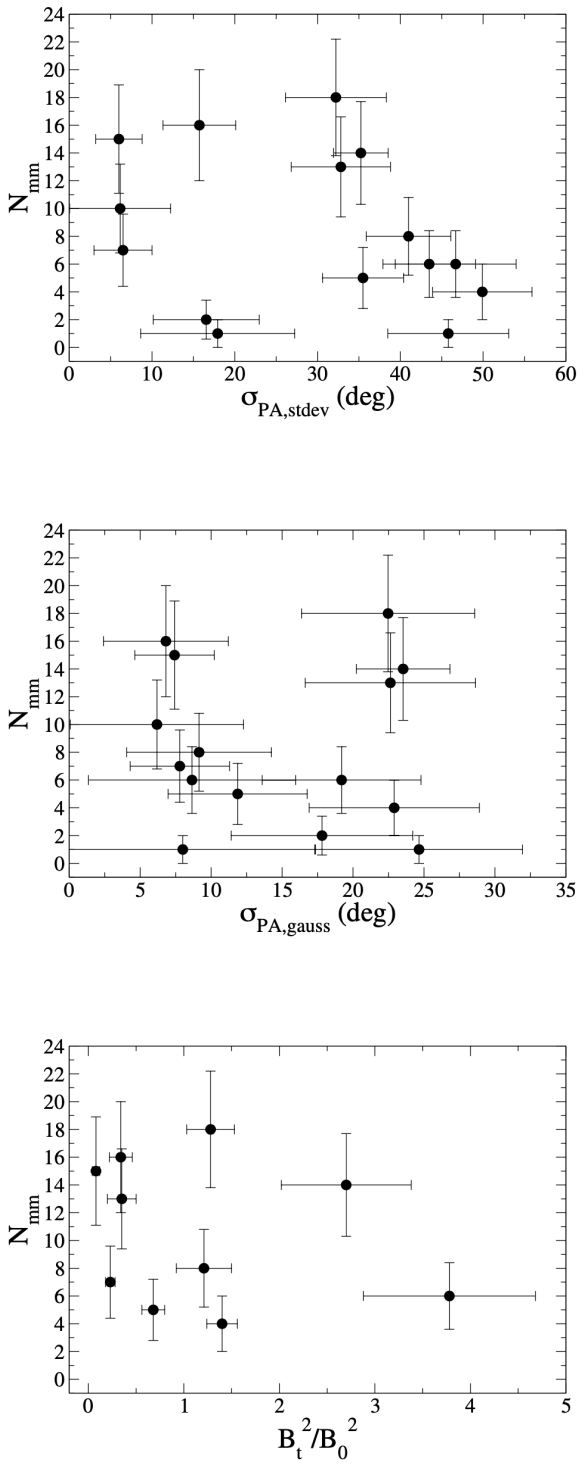

FIG. 6.— Top: Fragmentation level vs polarization PA intrinsic standard deviation of the weighted mean (Section 4.3.1). Middle: Fragmentation level vs polarization PA dispersion after fitting multiple PA components in the PA histograms (Section 4.3.2). Bottom: Fragmentation level vs energy ratio between the perturbed magnetic field and the large-scale ordered magnetic field (Section 4.4).

our results. The advantage of using single-dish telescopes to infer the density structure is that the temperature structure can be better determined thanks to the simultaneous fitting of the SED and the radial intensity profiles.

Regarding the estimate of the velocity dispersion, the $H^{13}CO^+$ (4–3) transition was used. This is a good tracer of dense regions, which should correlate well with the polarized emission, as shown in Figs. 14a and 14b of the Appendix. However, both the velocity dispersion and the PA dispersion could still be affected by the presence of outflows. As shown in Figs. 14a and 14b, the magnetic field is, for most of the cases, perpendicular to the outflows directions, with the only clear exception of N6334In. Other cases where the polarized emission seems to follow the outflow directions are DR21OH and N48. In none of the regions there is evidence of the magnetic field segments being especially perturbed along the outflow directions. Thus, it is unlikely that the velocity and PA dispersions are strongly affected by outflows.

Regarding the estimate of the PA dispersion, the DCF method tends to overestimate the magnetic field strengths (Heitsch et al. 2001) in cases of weak magnetic fields or super-Alfvénic conditions. These conditions could be easily fulfilled in presence of bulk motions of gas flowing towards the center of the massive dense cores (e. g., Csengeri et al. 2011, Lee et al. 2013, Battisti & Heyer 2014, Liu et al. 2015, Motte et al. 2018, Schwörer et al. 2019). Actually, the morphology of the magnetic field segments in several regions studied here suggests such kind of motions (see, for example, the cases of W3IRS5, N6334V, W75N, DR21OH, and N48 in

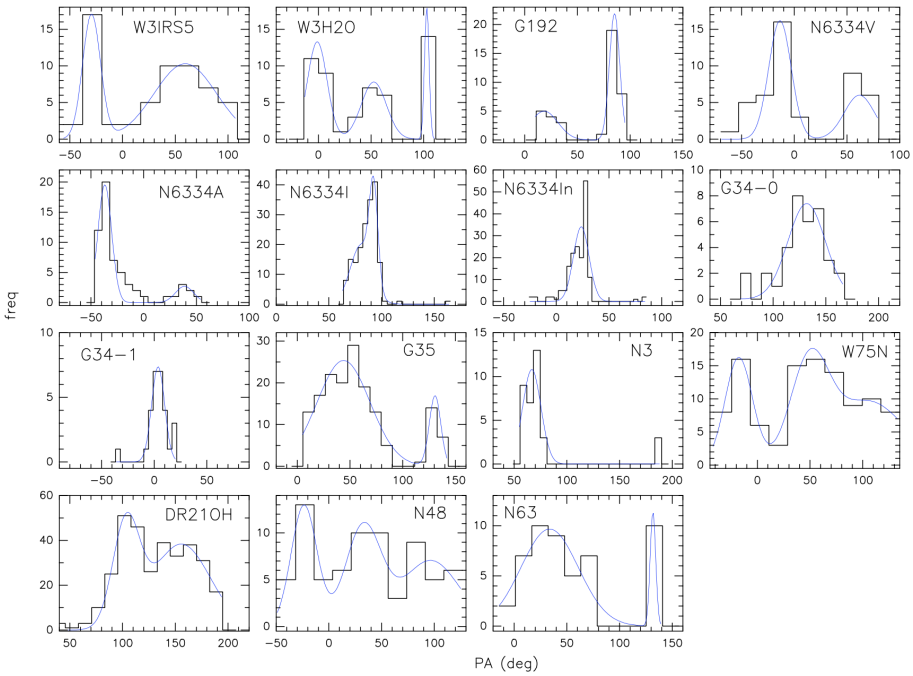

FIG. 7.— Polarization angle histograms (black) with the gaussian fits (blue curves) performed in Python to estimate the PA dispersion in each region. In all panels the full range of 180° is shown.

Figs. 2a and 2b). In these cases, the DCF method would overestimate the magnetic field strength because energy equipartition (a basic assumption of the DCF method) might not be reached if the magnetic field does not follow the strong kinetic motions. We explored this possibility for the particular case of N6334V, where simulations of a collapsing magnetized molecular cloud were specifically tuned to explain the magnetic field and dynamics of the region (Juárez et al. 2017). In these simulations, the gas flows from the large scales towards the center of the massive dense cores, and the magnetic field is dragged by the gas. The magnetic field in the simulations was measured within 0.15 pc of the massive dense core and a value of 0.94 mG was found (Zamora-Avilés, priv. communication), very similar to the value obtained here for N6334V using the 'standard deviation' approach, of $\sim$ 0.8 mG, and only a factor of 2 smaller than the magnetic field strength obtained using the ADF method. Thus, for the particular case of N6334V, the magnetic field measured in the simulations is very comparable to the magnetic field inferred in our work using the DCF method.

We should remind also that the measured PA dispersion can be underestimated due to the finite angular resolution, averaging along the line of sight (although these two effects are already taken into account in the ADF method), or superposition with a strong and uniform large-scale field, yielding in all these cases to an overestimation of the magnetic field strength. In the ADF method, $\langle B_t^2\rangle/\langle B_0^2\rangle$ could be underestimated for the cases of very weak magnetic fields. In these cases the magnetic field could be so strongly perturbed that it could resemble a random field with no important changes with distance, implying an overestimation of the large-scale ordered field. However, such an extreme disordered and random-like magnetic field is not seen in our observations (Figs. 2a and 2b).

A final way to test how robust is our determination of the magnetic field strength is to compare it to other values reported in the literature, especially when completely independent methods are used, such as the ion-neutral drift (see below). In Table 4, the magnetic field obtained in other works in the literature are reported (see table notes of Table 4 for a reference to the different methods). For example, Hezareh et al. (2010, 2013) estimated the magnetic field in the DR21 region, including DR21OH, N3 and N53, by comparing the velocity dispersions of ion and neutral pairs at different length scales, and find values in the range 0.33–1.8 mG (for densities very similar to the ones we obtained here). Li et al. (2015) present evidence that magnetic fields regulate the dynamics in NGC 6334, based on their findings of hourglass-shaped field lines at gas column density peaks and from the fact that the field strength is found to be proportional to the 0.4-power of the density. They infer the magnetic field strength by assuming force equilibrium between gravity, magnetic tension and magnetic pressure at different scales, and derive a relation between magnetic field strength and density. The value given in Table 4 for the magnetic field strength in N6334I and N6334In is the one corresponding to the density given in Table 3 and applying the aforementioned relation between field strength and density. For the G34 cores, Tang et al. (2019) also report submillimeter polarization observations using the Caltech Submillimeter Observatory and infer the magnetic field strength using the ADF method for both G34-0 and G34-1 (Table 4; Tang et al. (2019) report densities of 1.6×10^5 cm^{-3} for these two cores). Regarding W3H2O, Chen et al. (2012b) estimate the magnetic field strength using the DCF method with a density of 1.5×10^7 cm^{-3}, and obtained 17 mG. To compare this value to our measurement, we scaled the magnetic field strength assuming a dependence with density as a power law with index 0.4 (Li et al. 2015), and used our estimate for the density reported in Table 3, obtaining a value of 4.6 mG. For the case of G35, Qiu et al. (2013) report a value

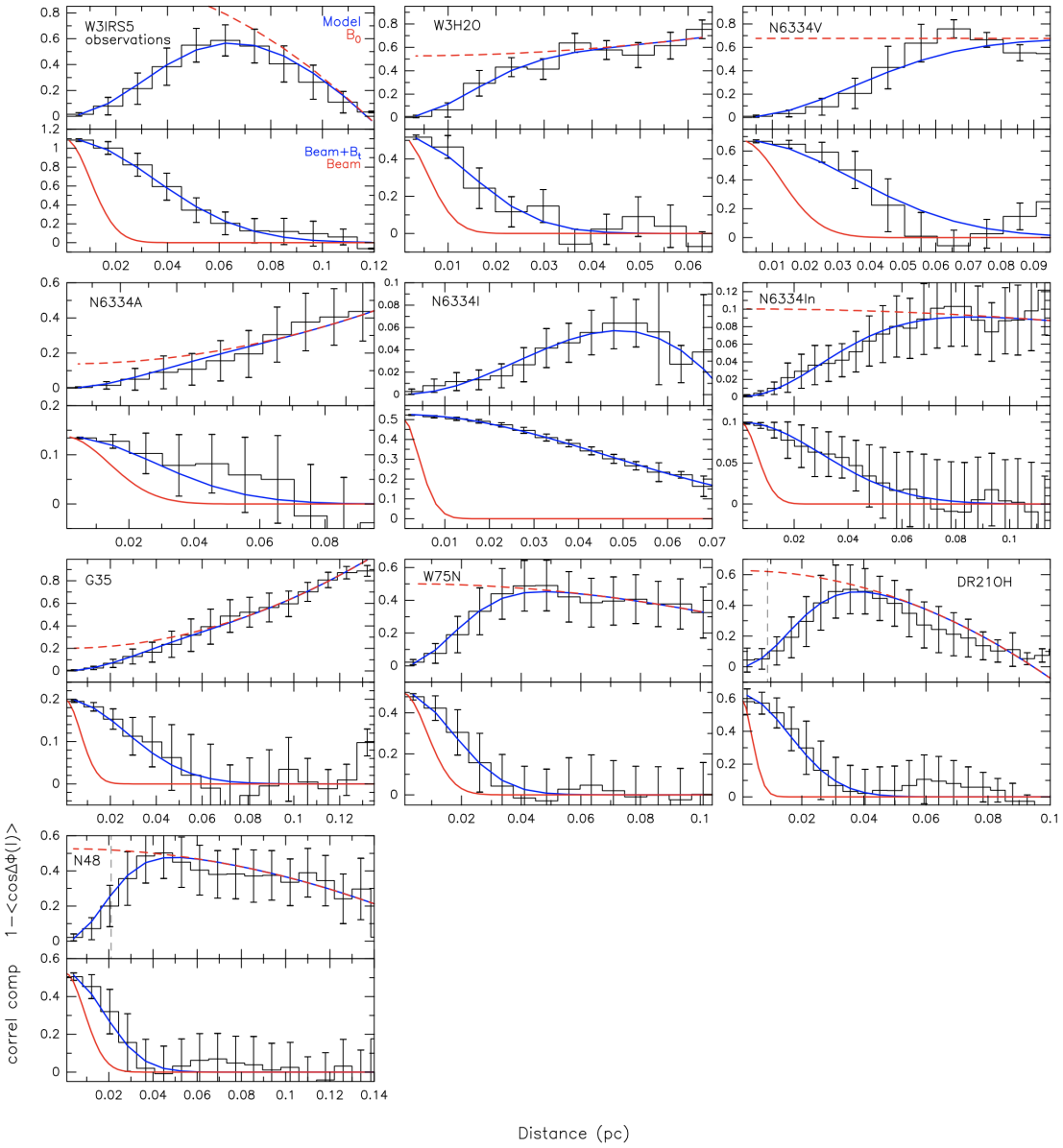

FIG. 8.— Results of the ADF method for each region with enough polarization detections. For each region, the top panel corresponds to the ADF ($1-\langle\cos[\Delta\Phi(l)]\rangle$) and the bottom panel corresponds to the correlated component (exponential term of equation (3)). In both upper and lower panels, the black solid line and error bars correspond to the mean and standard deviation of all the pairs in each bin. The red dashed line corresponds to the large-scale uniform magnetic field (i. e., it does not contain the correlated component of the function and is $b/N + a_2' l^2$). In the upper panel, the blue line shows the fit to the data using equation (3), and in the bottom panel the blue line shows the correlation due to the beam and the turbulent component of the magnetic field, while the solid red line corresponds to the correlation due to the beam alone.

of the magnetic field strength of 0.9–1.4 using the same SMA dataset used in this work and the ADF method. Last, I20126 has been observed with the SMA in submillimeter polarization but no sufficient detections were found to estimate a reliable PA dispersion (Shinnaga et al., in preparation). However, Edris et al. (2005) perform estimates of the magnetic field at scales of $\sim$ 1000 AU through Zeeman splitting of OH masers, and obtain 11 mG within 0.5″. Assuming that the density at $\sim$ 1000 AU is around 8.4×10^{-17} g cm^{-3} (Table 3), we estimate a magnetic field strength of 1.8 mG for the density we have calculated within 0.15 pc.

Fig. 17 of the Appendix shows that the relation between the magnetic field strength reported in the literature and the strength derived in this work is quite close to the one-to-one relation. The cases of N6334I, N6334In, DR21OH, and N3 are particularly significant, as the methods used in the literature for these regions are independent to the method used here. This figure indicates that the method used here to infer the magnetic field strength is reasonable.

In addition to all the uncertainties mentioned above, a number of caveats have been raised in the literature regarding the DCF method, for which several corrections have been proposed (Heitsch et al. 2001; Falceta-Gonçalves et al. 2008; Hildebrand et al. 2009; Houde et al. 2009, 2011; Franco et al. 2010; Koch et al. 2010). One of the main caveats is related to the small angle approximation assumed in the original DCF method. For this reason, we applied the correction by Falceta-Gonçalves et al. (2008) in our determination of

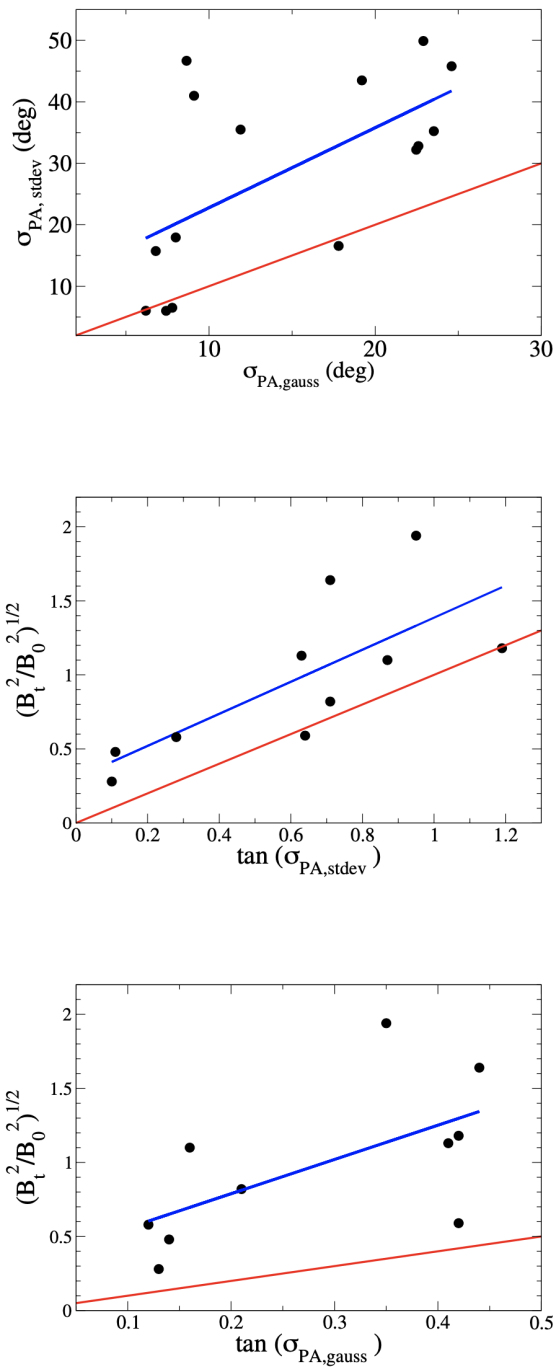

FIG. 9.— Top: PA dispersion obtained using the standard deviation approach, $\sigma_{\rm PA,stdev}$, vs PA dispersion obtained using the multiple gaussian approach, $\sigma_{\rm PA,gauss}$. Middle: $(\langle B_{\rm t}^2\rangle/\langle B_0^2\rangle)^{1/2}$ vs tan($\sigma_{\rm PAstdev}$). Bottom: $(\langle B_{\rm t}^2\rangle/\langle B_0^2\rangle)^{1/2}$ vs tan($\sigma_{\rm PA,gauss}$). In all three panels, the blue line indicates the resulting linear fit to the data, and the red line corresponds to the one-to-one relation.

the magnetic field strength (see Section 4.5). The other corrections typically imply a factor well below 4 (see Cortés et al. 2016, 2019 for a comparison among the values obtained using the different corrections).

Finally, it is important to note that the fact that $\sigma_{\rm PA,stdev}$ correlates well with $\langle B_{\rm t}^2\rangle/\langle B_0^2\rangle$ obtained from the ADF method (Fig.9 of the Appendix) is indicative of our determination of the magnetic field strength being fair. Such a correlation is a significant result because the ADF method does not suffer from the biases described in Section 4.4 and its robustness has been tested by Liu et al. (2019). These authors find that, although this approach has large uncertainties, it yields no more than a factor of 2 of difference with respect to other approaches (such as the structure function and unsharp masking). The problem with the ADF is that it can only be applied to regions with a very large number of polarization PA detections. In our case, the ADF approach could be applied only to 10 out of the 15 regions with polarization detections. Thanks to the correlation found between $\sigma_{\rm PA,stdev}$ and $\langle B_{\rm t}^2\rangle/\langle B_0^2\rangle$, we can trust the estimate of $\sigma_{\rm PA,stdev}$, which, in turn, can be applied to a larger number of regions, allowing us to improve the statistics to test the $N_{\rm mm}$ vs $B_{\rm stdev}$ relation.

In spite of all the aforementioned caveats, the crucial aspect of the analysis presented here is that it is performed uniformly for the entire sample, measuring each parameter using exactly the same method and within the same field of view for all the regions. Hence our reported values of the magnetic field strength should be useful to assess the variation of the magnetic field in this sample.

5.2. *Possible trend with density within 0.15 pc*

In the top panel of Fig. 5, a possible correlation between the fragmentation level and the density averaged within 0.15 pc was found. Because we determined the density for a fixed size, such a relation with density is equivalent to a relation with mass. A linear regression fit gives a correlation coefficient of 0.68. The relation is consistent with previous observational studies (e. g., Gutermuth et al. 2011; Palau et al. 2014; Lee et al. 2015; Liu et al. 2016; Nguyen-Luong et al. 2016; Pokhrel et al. 2016, 2018; Mercimek et al. 2017; Alfaro & Román-Zúñiga 2018; Mendigutía et al. 2018; Murillo et al. 2018; Li et al. 2019; Lin et al. 2019; Orkisz et al. 2019; Sanhueza et al. 2019; Sokol et al. 2019; Svoboda et al. 2019; Zhang et al. 2019) and theoretical/numerical studies (Guszejnov et al. 2018; Burkhart et al. 2018; Dobbs et al. 2019) reporting an important role of density in determining fragmentation of massive dense cores, and is expected for the case of thermal Jeans fragmentation.

5.3. *Interplay between density and the magnetic field strength*

The lack of correlation between the fragmentation level and the magnetic field strength or the mass-to-flux over critical mass-to-flux ratio could be due to the fact that our sample is including massive dense cores with a too broad range of densities. In other words, since density and magnetic field could both affect the fragmentation level simultaneously, we consider here whether a relation is found when only regions with very similar densities are considered. Looking at Fig. 5-top, the range (4–8)×10^5 cm^{-3} includes a large number of regions and could be good to perform the aforementioned test. In Fig. 11 we present a plot of $N_{\rm mm}$ vs $B_{\rm stdev}$ only for the regions within the narrow density range given above. The figure presents hints of a possible anticorrelation between $N_{\rm mm}$ and $B_{\rm stdev}$, as expected if the magnetic field is effective at suppressing fragmentation. In turn, the different magnetic field strengths in the cores with similar density could explain the considerable scatter in the $N_{\rm mm}$ vs $n_{\rm 0.15pc}$ relation. What we find here is in full agreement with a recent work towards the infrared dark cloud G14.225−0.506, where the two main hubs of the cloud have very similar densities, and their different

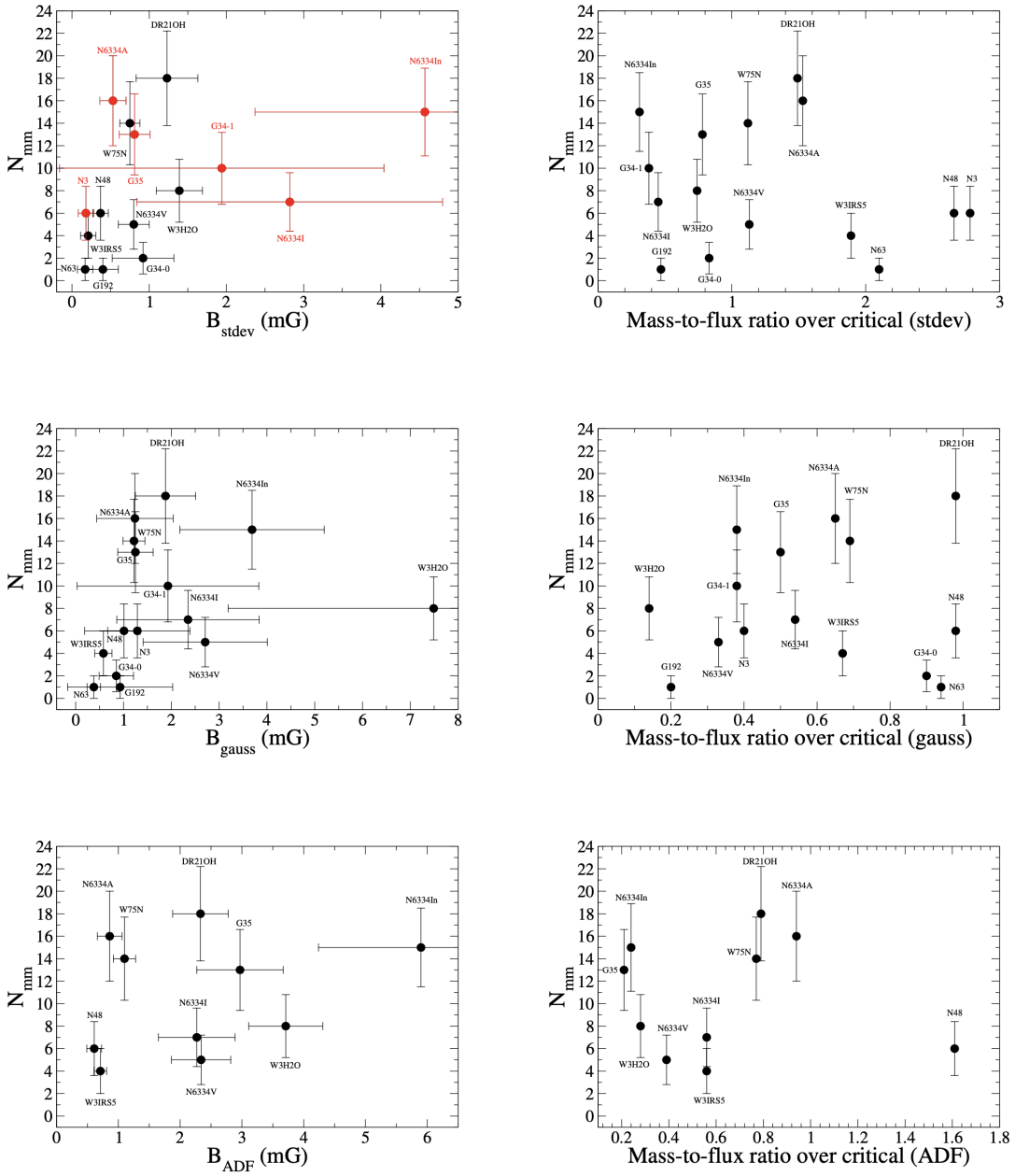

FIG. 10.— The three panels on the left show the plots of $N_{\rm mm}$ vs the magnetic field strength for the different approaches used in this work: 'standard deviation' ($B_{\rm stdev}$, top), 'multiple gaussian' ($B_{\rm gauss}$, middle), and ADF ($B_{\rm ADF}$, bottom). In the top-left panel, the red dots correspond to the cores classified as 'aligned fragmentation'. The three panels on the right show the plots of $N_{\rm mm}$ vs the ratio of mass-to-flux to critical mass-to-flux for the same three approaches.

fragmentation levels can be explained with the different measured magnetic field strengths (Añez-López et al. 2020b).

5.4. *Comparison of average fragment masses with Jeans and critical masses*

The fact that the $N_{\rm mm}$ vs $n_{0.15{\rm pc}}$ relation is stronger than the $N_{\rm mm}$ vs $B_{\rm stdev}$ relation suggests that thermal Jeans fragmentation has a non-negligible role in the fragmentation of our sample. If this is the case, the mass of the fragments should be comparable to the Jeans mass. Using the density and temperature averaged within 0.15 pc reported in Table 3, we calculated the Jeans mass following equation (6) of Palau et al. (2015). The values of the Jeans mass for each massive dense core, $M_{\rm Jeans}$, are reported in Table 2. As can be seen from this table, $M_{\rm Jeans}$ is of the order 1–5 $M_\odot$, very similar to the average mass of the fragments in each core.

The critical mass for magnetic support were calculated for completeness following equation (16) of McKee & Ostriker (2007), listed in Table 2. These critical masses are of the order of 10–100 $M_\odot$, about one order of magnitude larger than the average mass of the fragments in each core. These calculations suggest again that the fragmentation process in our sample is consistent with the thermal Jeans instability.

5.5. *Fragment sizes vs magnetic field strength*

We explore here whether there is any relation between the sizes of the fragments and the magnetic field strength of their parental core. Fig. 12 presents a plot with the 3σ radii for all

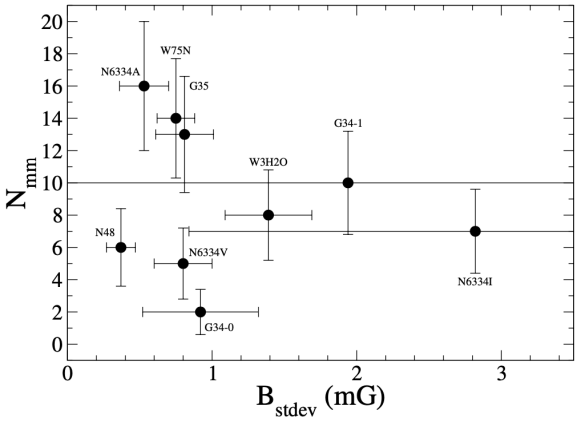

FIG. 11.— Fragmentation level vs magnetic field strength for regions with density in the range (4–8)×10^5 cm^{-3}.

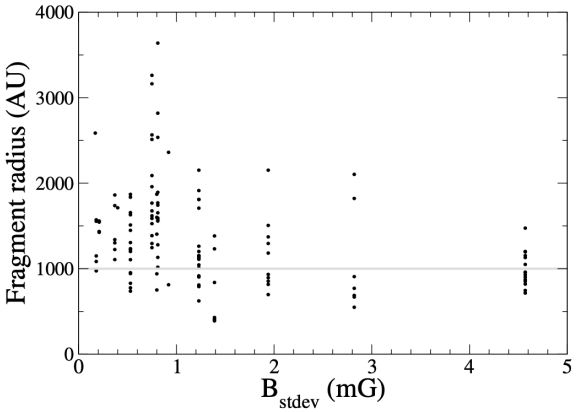

FIG. 12.— Radii (at the 3σ contour) of the fragments identified within each massive dense core vs magnetic field strength. The horizontal line indicates the typical spatial resolution of our observations (Table 1).

the 126 detected fragments vs the magnetic field strength. The figure indicates that there could be an upper envelope with the largest fragments tending to occur where the magnetic field is weaker. In addition, the scatter in the size of the fragments appears to decrease with growing field strength. For the largest field strength (corresponding to N6334In), the scatter appears to be very small (although statistics are not very large, see the standard deviations of the fragment sizes for each region in Table 2). Assuming that a fragment under a strong magnetic field is not accreting material from its surroundings as efficiently as a fragment under a weak magnetic field (because the magnetic field should slow the collapse down), the smaller sizes observed for regions with larger magnetic fields could indicate that the magnetic field is preventing these fragments from a fast growing in both mass and size.

In addition, the three regions with strongest magnetic field, N6334In, N6334I, and G34-1, have their fragments aligned along a prevailing direction, and as such they were classified as undergoing 'aligned fragmentation' in Table 2. This finding is fully consistent with the work of Fontani et al. (2018), who also report that a filamentary distribution of the fragments is favored for strong magnetic fields. For all these 3 cases, the magnetic field morphology is rather uniform and perpendicular to the axis of the aligned fragments. With such a geometry, and with a relatively strong magnetic field strength, the fragmentation process should happen along the field lines with material moving more easily along the field lines from the outer regions towards a mid-plane. This could explain the relatively small scatter in size for such a configuration. Note that G35 also presents 'aligned fragmentation', but has the magnetic field along the main axis of the filamentary structure, its magnetic field strength is relatively low, and presents a large scatter in the fragment sizes (Table 2), thus also fitting within this picture. In summary, the magnetic field strength, the small scatter in the sizes of the fragments, and the field morphology all suggest that the magnetic field in these three cases is regulating at least partially the fragmentation process.

5.6. *Implications of our results*

As mentioned in the introduction, a number of theoretical and numerical studies suggest that magnetic fields could be crucial to determine the fragmentation level of molecular clumps and cores, because strong magnetic fields should suppress fragmentation. In a recent review about the role of magnetic fields in the formation of molecular clouds, Hennebelle & Inutsuka (2019), present the assumptions leading to ideal MHD equations, taking into account ion-neutral drift. They consider the influence that the magnetic field may have on the interstellar filaments and the molecular clouds, and its role on the formation of stellar clusters. They argue that the magnetic field could be responsible for reducing the star formation rate and the numbers of clumps, cores and stars.

In this paper we aimed at testing this from direct observations. From our uniform analysis of the entire sample of 17 massive dense cores at $\sim$ 0.15 pc scales, no clear hints of the expected relation of higher fragmentation with fainter magnetic field strengths were found. In particular, we find at least three cores (N63, G192 and G34-0) with very little fragmentation and very small magnetic field strengths. On the other hand, a possible relation between fragmentation level and density (within 0.15 pc) is apparent from our analysis (Section 5.2), and the average mass of the fragments in each region is comparable to the Jeans mass. These two observational findings suggest that the fragmentation process in our sample is mainly dominated by gravity. This is consistent with very recent numerical simulations from Krumholz & Federrath (2019), who find that the magnetic field strength should not strongly affect the star formation rate or initial mass function in star-forming clouds at their earliest stages of formation.

It is worth mentioning that the magnetic field strengths inferred in this work cover a range of about one order of magnitude (from 0.2 to 4.6 mG, or μ from 0.3 to 2.8), and are also subject to a number of uncertainties (see Section 5.1), while simulations showing very different fragmentation levels correspond to setups differing by two orders of magnitude in the mass-to-flux vs critical mass-to-flux ratio (e. g., from 2 to 130, Hennebelle et al. 2011; Commerçon et al. 2011). This suggests that the typical magnetic fields in the massive dense cores of our sample do not cover a sufficiently large range to leave a clear trace on the fragmentation level and that this is rather determined by other environmental factors such as density.

However, finer details of our observational dataset seem to be consistent with the magnetic field affecting the fragmentation process at least partially. First, when considering only

the regions with similar density, we did find a possible anti-correlation between $N_{\rm mm}$ and the magnetic field strength, as expected theoretically and numerically. This could explain the significant scatter found in the $N_{\rm mm}$ vs density relation. Second, the regions with strongest magnetic field (N6334I, N6334In, and G34-1) undergo fragmentation along a preferential direction, which is perpendicular to the magnetic field lines. Third, the three regions with strongest magnetic fields are also the regions with small fragments and with almost all fragments with similar sizes. These three findings suggest that the magnetic field, at least in these three cases, is somehow affecting the fragmentation process. It is therefore necessary to test this in a larger sample to strengthen the hints found here.

6. CONCLUSIONS

We have compiled a sample of 17 massive dense cores for which submillimeter polarization observations from the Legacy Program of the SMA (Zhang et al. 2014), as well as submillimeter continuum images at high angular resolution were available. The sample was built to strictly fulfill constraints of spatial resolution of $\sim$ 1000 AU and mass sensitivities (from the submillimeter continuum) around $\sim$ 0.5 $M_{\odot}$, so that a fragmentation level can be measured in a uniform and reliable way (and within the same field of view of 0.15 pc) for all the cores. The polarization images were analyzed to infer polarization position angle (PA) dispersions. In addition, $H^{13}CO^{+}$ (4–3) data from the SMA observations were used to infer velocity dispersions for each core. Finally, the temperature and density structure were modeled for each massive dense core using submillimeter continuum emission from single-dish telescopes and the Spectral Energy Distribution, following Palau et al. (2014). All the quantities were measured in a uniform way and within the same field of view of 0.15 pc. The aforementioned inferred properties of the massive dense cores allowed us to calculate magnetic field strengths using the DCF and ADF methods, and search for possible trends between the fragmentation level and any of the derived properties of the parental cores. Our main conclusions can be summarized as follows:

- A total number of 126 fragments have been identified within the 17 massive dense cores. We have assigned a fragmentation level within a field of view of 0.15 pc, $N_{\rm mm}$, to each massive dense core. We found a variety of fragmentation levels, with 22% of the cores presenting almost no fragmentation, and 39% of the cores presenting a high fragmentation level. Additionally, cores were classified according to their fragmentation type, mainly 'aligned fragmentation' (6 cores), 'clustered fragmentation' (6 cores) and 'no fragmentation' (4 cores).

- The inferred power-law indices for the density of the massive dense cores range from 1.46 to 2.26. The densities, masses, and temperatures, all (averaged) within 0.15 pc, range from 1.1 to 10.5 $\times 10^5$ cm^{-3}, from 11 to 105 $M_{\odot}$, and from 23 to 120 K, respectively. A correlation was found between the fragmentation level and the density averaged within 0.15 pc.

- The line widths of the $H^{13}CO^{+}$ (4–3) transition measured in each core range from 1.3 to 9.7 km s^{-1}, and no clear trend was found between $N_{\rm mm}$ and these line widths.

- Two approaches were used to estimate polarization PA dispersions. First, the PA dispersion was estimated from the standard deviation of the PA corrected for the PA uncertainties. Second, different Gaussians were fitted to the PA histograms. Additionally, the Angular Dispersion Function analysis was performed following Houde et al. (2009). It was found that the PA dispersion, inferred from the standard deviation, correlates with the corresponding quantity from the ADF analysis, and the first one was used as reference to calculate the magnetic field strengths. PA dispersions ranged from 6 to 50°. In combination with the line widths and average densities, this yielded magnetic field strengths ranging from 0.2 to 4.6 mG.

- When considering the entire sample, no obvious relation was apparent between $N_{\rm mm}$ and the magnetic field strength or the mass-to-flux over critical mass-to-flux ratio. However, when considering the cores with similar densities, hints of an anticorrelation of $N_{\rm mm}$ with the magnetic field strength were found, suggesting that for cores with similar density, the magnetic field suppresses fragmentation, as suggested by a number of theoretical and numerical works.

- The sizes and masses of each fragment were measured. The average masses of the fragments ranged from 2–5 $M_{\odot}$ in most cases, which are comparable to the thermal Jeans mass. On the other hand, the average masses of the fragments were one order of magnitude smaller than the magnetic critical mass. Regarding the sizes of the fragments, hints of more compact fragments for stronger magnetic fields were found, suggesting that in the cases of strong magnetic field this might slow down the accretion process compared to the non-magnetic case. In addition, for the strong magnetic field cases, fragmentation seems to take place along a preferred direction perpendicularly to the magnetic field.

In summary, our entire sample of massive dense cores presents a relation of the fragmentation level with the density of the parental core, while no clear trend is found with the magnetic field strength. Furthermore, the average mass of the fragments is comparable to the thermal Jeans mass. However, the trend between fragmentation level and density has a significant scatter, and this could be explained by the different magnetic field strengths in cores with similar densities. In addition, hints were found of the magnetic field influencing the fragmentation process for the cores with strongest magnetic fields. Overall, the observed properties of our sample are consistent with thermal Jeans fragmentation, and the magnetic field seems to act as a modulating process required to explain the finer details of the fragmenting cores.

AP is grateful to Manuel Zamora-Avilés for calculating the magnetic field strength within a region of 0.15 pc of diameter in the simulations of Juárez et al. (2017) of N6334V, to Javier Ballesteros-Paredes for very insightful discussions, and to Daniel J. Díaz González for useful support using Python. AP acknowledges financial support from CONACyT and UNAM-PAPIIT IN113119 grant, México. JMG and RE are supported by the Spanish grant AYA2017-84390- C2-R (AEI/FEDER, UE). JL and KQ are supported by National Key R&D Program of China No. 2017YFA0402600. JL and KQ acknowledge the support from National Natural Science Foundation of China (NSFC) through grants U1731237, 11590781,

and 11629302. PMK acknowledges support from Ministery of Science and Technology (MoST) grants MOST 108-2112-M-001-012 and MOST 107-2119-M-001-023 in Taiwan, and from an Academia Sinica Career Development Award. ZYL is supported in part by NSF AST-1716259 and 1815784. LAZ is grateful to CONACyT, México, and DGAPA, UNAM for their financial support.

Part of the data used in this paper were obtained in the SMA legacy project: Filaments, Magnetic Fields, and Massive Star Formation (PI: Qizhou Zhang). This research made use of Astropy[20], a community–developed core Python package for Astronomy (AstropyCollaboration et al. 2013; Price-Whelan et al. 2018), and in particular the numpy (van der Walt et al. 2011). The Karma software was used for part of the analysis of this paper (Gooch 1996).

REFERENCES

Adams, F. C. 1991, ApJ, 382, 544
Ahmadi, A., Beuther, H., Mottram, J. C., et al. 2018, A&A, 618, A46
Alfaro, E. J., & Román-Zúñiga, C. G. 2018, MNRAS, 478, L110
Añez-López, N., Osorio, M., Busquet, G., et al. 2020a, ApJ, 888, 41
Añez-López, N., Busquet, G., Koch, P. M., Girart, J. M., Liu, H. B., Santos, F., Chapman, N. L., Novak, G., Ho, P. T. P., Palau, A., Zhang, Q. 2020b, A&A, submitted
Astropy Collaboration et al., 2013, A&A, 558, A33
Bailey, N. D., & Basu, S. 2012, ApJ, 761, 67
Battisti, A. J., & Heyer, M. H. 2014, ApJ, 780, 173
Beuther, H., Mottram, J. C., Ahmadi, A., et al. 2018, A&A, 617, A100
Bontemps, S., Motte, F., Csengeri, T., & Schneider, N. 2010, A&A, 524, A18
Boss, A. P. 1999, ApJ, 520, 744
Boss, A. P. 2004, MNRAS, 350, L57
Boss, A. P., & Bodenheimer, P. 1979, ApJ, 234, 289
Boss, A. P., & Keiser, S. A. 2013, ApJ, 764, 136
Boss, A. P., & Keiser, S. A. 2014, ApJ, 794, 44
Burkert A., Bate M. R., Bodenheimer P., 1997, MNRAS, 289, 497
Burkhart, B. 2018, ApJ, 863, 118
Busquet, G., Estalella, R., Palau, A., et al. 2016, ApJ, 819, 139
Cesaroni, R., Galli, D., Neri, R., et al. 2014, A&A, 566, A73
Chandrasekhar, S., & Fermi, E. 1953, ApJ, 118, 113
Chandler, C. J., Barsony, M., & Moore, T. J. T. 1998, MNRAS, 299, 789
Chen, X., Arce, H. G., Dunham, M. M., & Zhang, Q. 2012a, ApJ, 747, L43
Chen, H. H.-H., Pineda, J. E., Offner, S. S. R., et al. 2019, ApJ, 886, 119
Chen, H.-R., Rao, R., Wilner, D. J., Liu, S.-Y. 2012b, ApJ, 751, L13
Ching, T.-C., Lai, S.-P., Zhang, Q., et al. 2017, ApJ, 838, 121
Commerçon, B., Hennebelle, P., & Henning, T. 2011, ApJ, 742, L9
Cortes, P. C., Girart, J. M., Hull, C. L. H., et al. 2016, ApJ, 825, L15
Cortes, P. C., Hull, C. L. H., Girart, J. M., et al. 2019, ApJ, 884, 48
Crutcher, R. M., Nutter, D. J., Ward-Thompson, D., et al. 2004, ApJ, 600, 279
Csengeri, T., Bontemps, S., Schneider, N., et al. 2011, ApJ, 740, L5
Cunningham, A. J., Krumholz, M. R., McKee, C. F., et al. 2018, MNRAS, 476, 771
Davis, L. 1951, Phys. Rev., 81, 890, doi: 10.1103/PhysRev.81.890.2
Di Francesco, J., Johnstone, D., Kirk, H., MacKenzie, T., & Ledwosinska, E. 2008, ApJS, 175, 277
Dobbs, C. L., Rosolowsky, E., Pettitt, A. R., et al. 2019, MNRAS, 485, 4997
Duarte-Cabral, A., Bontemps, S., Motte, F., et al. 2013, A&A, 558, A125
Duarte-Cabral, A., Bontemps, S., Motte, F., et al. 2014, A&A, 570, A1
Edris, K. A., Fuller, G. A., Cohen, R. J., et al. 2005, A&A, 434, 213
Falceta-Gonçalves, D., Lazarian, A., & Kowal, G. 2008, ApJ, 679, 537
Federrath, C., Klessen, R. S., & Schmidt, W. 2008, ApJ, 688, L79
Fontani, F., Commerçon, B., Giannetti, A., et al. 2016, A&A, 593, L14
Fontani, F., Commerçon, B., Giannetti, A., et al. 2018, A&A, 615, A94
Forgan, D., & Rice, K. 2012, MNRAS, 420, 299
Franco, G. A. P., Alves, F. O., & Girart, J. M. 2010, ApJ, 723, 146
Galametz, M., Maury, A., Girart, J. M., et al. 2018, A&A, 616, A139
Girart, J. M., Frau, P., Zhang, Q., et al. 2013, ApJ, 772, 69
Girichidis, P., Federrath, C., Banerjee, R., & Klessen, R. S. 2011, MNRAS, 413, 2741
Girichidis, P., Seifried, D., Naab, T., et al. 2018, MNRAS, 480, 3511
Gooch, R. 1996, in ASP Conf. Ser. 101, Astronomical Data Analysis Softwareand Systems V, ed. G. H. Jacoby & J. Barnes(Tucson, AZ: ASP),80
Guszejnov, D., Hopkins, P. F., Grudić, M. Y., et al. 2018, MNRAS, 480, 182
Gutermuth, R. A., Pipher, J. L., Megeath, S. T., et al. 2011, ApJ, 739, 84
Heitsch, F., Zweibel, E. G., Mac Low, M.-M., et al. 2001, ApJ, 561, 800
Hennebelle, P., Commerçon, B., Joos, M., et al. 2011, A&A, 528, A72
Hennebelle, P., & Inutsuka, S.-. ichiro . 2019, Frontiers in Astronomy and Space Sciences, 6, 5
Hennebelle, P., Whitworth, A. P., Cha, S.-H., et al. 2004, MNRAS, 348, 687
Hezareh, T., Wiesemeyer, H., Houde, M., et al. 2013, A&A, 558, A45
Hezareh, T., Houde, M., McCoey, C., et al. 2010, ApJ, 720, 603

[20] http://www.astropy.org

Hildebrand, R. H., Kirby, L., Dotson, J. L., et al. 2009, ApJ, 696, 567
Houde, M., Rao, R., Vaillancourt, J. E., et al. 2011, ApJ, 733, 109
Houde, M., Vaillancourt, J. E., Hildebrand, R. H., et al. 2009, ApJ, 706, 1504
Juárez, C., Girart, J. M., Zamora-Avilés, M., et al. 2017, ApJ, 844, 44
Keto, E., Field, G. B., & Blackman, E. G. 2020, MNRAS, 492, 5870
Koch, P. M., Tang, Y.-W., & Ho, P. T. P. 2010, ApJ, 721, 815
Krumholz, M. R., & Federrath, C. 2019, Frontiers in Astronomy and Space Sciences, 6, 7
Lee, K. I., Dunham, M. M., Myers, P. C., et al. 2015, ApJ, 814, 114
Lee, K., Looney, L. W., Schnee, S., et al. 2013, ApJ, 772, 100
Li, H.-B., Yuen, K. H., Otto, F., Leung, P. K., Sridharan, T. K., Zhang, Q., Liu, H., Tang, Y.-W., Qiu, K. 2015, Nature, 520, 518
Li, J., Myers, P. C., Kirk, H., et al. 2019, ApJ, 871, 163
Lin, Y., Csengeri, T., Wyrowski, F., et al. 2019, A&A, 631, A72
Liu, T., Kim, K.-T., Yoo, H., et al. 2016, ApJ, 829, 59
Liu, H. B., Qiu, K., Zhang, Q., et al. 2013, ApJ, 771, 71
Liu, H. B., Galván-Madrid, R., Jiménez-Serra, I., et al. 2015, ApJ, 804, 37
Liu, J., Qiu, K., Berry, D., Di Francesco, J. et al. 2019, ApJ, 877, 43
Liu, J., Zhang, Q., Qiu, K., Liu, H. B., Pillai, T., Girart, J. M., et al. 2020, ApJ, submitted
Machida, M. N., Matsumoto, T., Hanawa, T., et al. 2005, MNRAS, 362, 382
Maury, A. J., André, P., Hennebelle, P., et al. 2010, A&A, 512, A40
McKee, C. F., & Ostriker, E. C. 2007, ARA&A, 45, 565
Mendigutía, I., Lada, C. J., & Oudmaijer, R. D. 2018, A&A, 618, A119
Mercimek, S., Myers, P. C., Lee, K. I., et al. 2017, AJ, 153, 214
Motte, F., Bontemps, S., Schilke, P., et al. 2007, A&A, 476, 1243
Motte, F., Bontemps, S., & Louvet, F. 2018, ARA&A, 56, 41
Murillo, N. M., van Dishoeck, E. F., Tobin, J. J., et al. 2018, A&A, 620, A30
Myers, A. T., McKee, C. F., Cunningham, A. J., et al. 2013, ApJ, 766, 97
Myhill, E. A., & Kaula, W. M. 1992, ApJ, 386, 578
Nguyen-Luong, Q., Nguyen, H. V. V., Motte, F., et al. 2016, ApJ, 833, 23
Orkisz, J. H., Peretto, N., Pety, J., et al. 2019, A&A, 624, A113
Ossenkopf, V., & Henning, T. 1994, A&A, 291, 943
Ostriker, E. C., Stone, J. M., & Gammie, C. F. 2001, ApJ, 546, 980
Padoan, P., & Nordlund, Å. 2002, ApJ, 576, 870
Palau, A., Ballesteros-Paredes, J., Vázquez-Semadeni, E., et al. 2015, MNRAS, 453, 3785
Palau, A., Estalella, R., Girart, J. M., et al. 2014, ApJ, 785, 42
Palau, A., Fuente, A., Girart, J. M., et al. 2013, ApJ, 762, 120
Palau, A., Sánchez-Monge, Á., Busquet, G., et al. 2010, A&A, 510, A5
Peretto, N., Hennebelle, P., & André, P. 2007, A&A, 464, 983
Peters, T., Banerjee, R., Klessen, R. S., et al. 2011, ApJ, 729, 72
Pokhrel, R., Gutermuth, R., Ali, B., et al. 2016, MNRAS, 461, 22
Pokhrel, R., Myers, P. C., Dunham, M. M., et al. 2018, ApJ, 853, 5
Price, D. J., & Bate, M. R. 2007, MNRAS, 377, 77
Price-Whelan A. M., et al., 2018, AJ, 156, 123
Qiu, K., Zhang, Q., Menten, K. M., et al. 2013, ApJ, 779, 182
Sanhueza, P., Contreras, Y., Wu, B., et al. 2019, ApJ, 886, 102
Santos, F. P., Busquet, G., Franco, G. A. P., et al. 2016, ApJ, 832, 186
Schmeja, S., & Klessen, R. S. 2004, A&A, 419, 405
Scoville, N. Z., & Kwan, J. 1976, ApJ, 206, 718
Sokol, A. D., Gutermuth, R. A., Pokhrel, R., et al. 2019, MNRAS, 483, 407
Svoboda, B. E., Shirley, Y. L., Traficante, A., et al. 2019, ApJ, 886, 36
Schwörer, A., Sánchez-Monge, Á., Schilke, P., et al. 2019, A&A, 628, A6
Tang, Y.-W., Koch, P. M., Peretto, N., et al. 2019, ApJ, 878, 10
Tigé, J., Motte, F., Russeil, D., et al. 2017, A&A, 602, A77
van der Walt S, Colbert SC, Varoquaux G. 2011, Comp. in Sci. and Eng.13:22
Vázquez-Semadeni, E., Kim, J., & Ballesteros-Paredes, J. 2005, ApJ, 630, L49
Vázquez-Semadeni, E., Passot, T., & Pouquet, A. 1996, ApJ, 473, 881
Vázquez-Semadeni, E., Banerjee, R., Gómez, G. C., et al. 2011, MNRAS, 414, 2511
Williams, J. P., Blitz, L., & McKee, C. F. 2000, Protostars and Planets IV, 97
Zapata, L. A., Rodríguez-Garza, C., Rodríguez, L. F., Girart, J. M., & Chen, H.-R. 2011, ApJ, 740, L19
Zhang, M., Kainulainen, J., Mattern, M., et al. 2019, A&A, 622, A52
Zhang, Q., Qiu, K., Girart, J. M., et al. 2014, ApJ, 792, 116
Zhang, Q., Wang, Y., Pillai, T., & Rathborne, J. 2009, ApJ, 696, 268
Zhang, Q., Wang, K., Lu, X., et al. 2015, ApJ, 804, 141
Ziegler, U. 2005, A&A, 435, 385

APPENDIX

TESTS FOR BIASES OF FRAGMENTATION LEVEL $N_{\rm mm}$

Fig. 13 presents the plots of $N_{\rm mm}$ (Section 3) vs the mass sensitivity and the spatial resolution for each region (both reported in Table 1). If $N_{\rm mm}$ were biased with these two quantities one would expected a large $N_{\rm mm}$ for smaller (better) mass sensitivities, and a large $N_{\rm mm}$ for smaller (better) spatial resolutions. As can be seen from the figure, none of these two biases affect our sample.

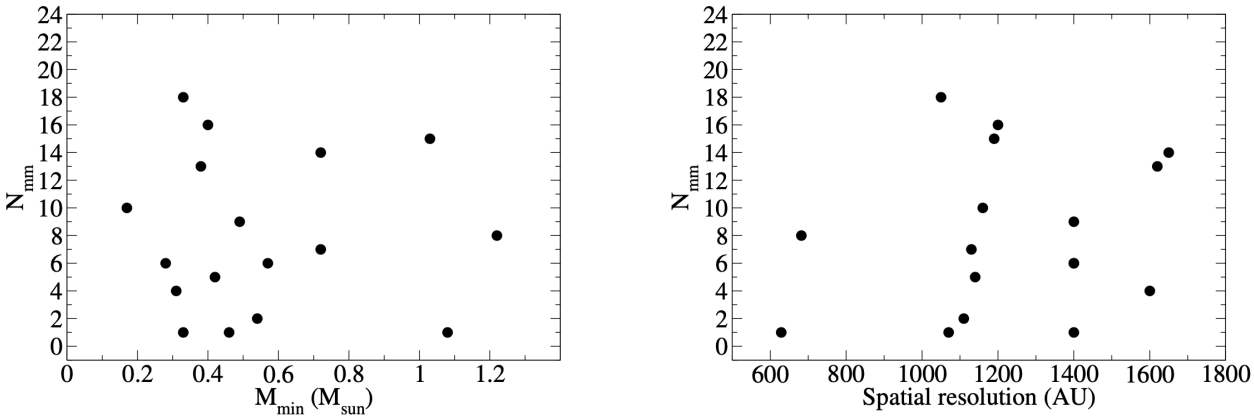

FIG. 13.— Left: Fragmentation level $N_{\rm mm}$ vs the mass sensitivity for each massive dense core. Right: Fragmentation level $N_{\rm mm}$ vs the spatial resolution for each massive dense core. These figures show that there are no biases of $N_{\rm mm}$ with respect to observational parameters, such as mass sensitivity and spatial resolution (both related to distance).

FIRST-ORDER MOMENTS FOR $H^{13}CO^+$ (4–3) DATA

Figs. 14a and 14b show the first-order moments of the $H^{13}CO^+$ (4–3) transition in colorscale, with the magnetic field segments overplotted as well as arrows for the known outflows in each core (taken from the literature).

PARTICULAR CASES IN THE DENSITY AND TEMPERATURE STRUCTURE MODELING OF SECTION 4.1

In Section 4.1 a density and temperature structure model was fit to observational data for each region of our sample. The observational data consisted of radial intensity profiles and the spectral energy distribution, and the model allowed us to infer an average density within 0.15 pc for each region. For two of the regions, we calculated a range of possible average densities within 0.15 pc (N6334A and G35). For the case of N6334A, the assumption of the core being centrally heated might not be fulfilled because there is a Herschel core (core number 38 from Tigé et al. 2017) that only lies about $\sim 13''$ from the SCUBA peak at 450 μm and for which the flux density at 70 μm is a factor of ~ 20 larger than the flux at 70 μm for the core directly associated with the 450 μm peak. In this case we used two approaches to estimate the radial density profile. First, to build the SED we considered only the Herschel intensities associated with core number 41 (core associated with the 450 μm peak). This yielded an average density within 0.15 pc of 5.9×10^5 cm^{-3}. This should be a reasonable approach as long as we are considering only peak intensities of the core directly associated with the SCUBA peak, and the excess due to heating by core 38 (and 10) should not be strong because its effect should be only in specific directions compared to the entire radially averaged profile. Second, we considered only the contribution of core 41 and used peak intensities to build the SED, except for Herschel wavelengths where the beam cannot separate the different sources (i. e., 250, 350 and 500 μm, where the beam is $> 12''$). For these wavelengths we included in the SED the flux density of all three cores and used the core size as aperture radius for the model to compute the flux. This method yielded an average density within 0.15 pc of 4.6×10^5 cm^{-3}, and in Table 3 we report the fitted values corresponding to this second method, to be conservative. In Fig. 5 we plot the average of these two possible densities. Regarding the case of G35, the IRAS flux at 100 μm is a factor of 3 smaller than the Herschel-PACS measurements at 70 and 160 μm. For this region, we calculated the model including both Herschel and IRAS fluxes (best-fit values reported in Table 3, yielding an average density within 0.15 pc of 3.6×10^5 cm^{-3}), and we also calculated the model including in the SED only the flux of IRAS at 100 μm and excluding PACS data (yielding an average density within 0.15 pc of 4.3×10^5 cm^{-3}). Fig. 5 presents the average of these possible densities.

MAGNETIC FIELD STRENGTH VS DENSITY

In Fig. 15 we present a plot of the magnetic field strength vs density averaged within 0.15 pc of diameter. The log-log plot shows a trend, with a slope of 1.2.

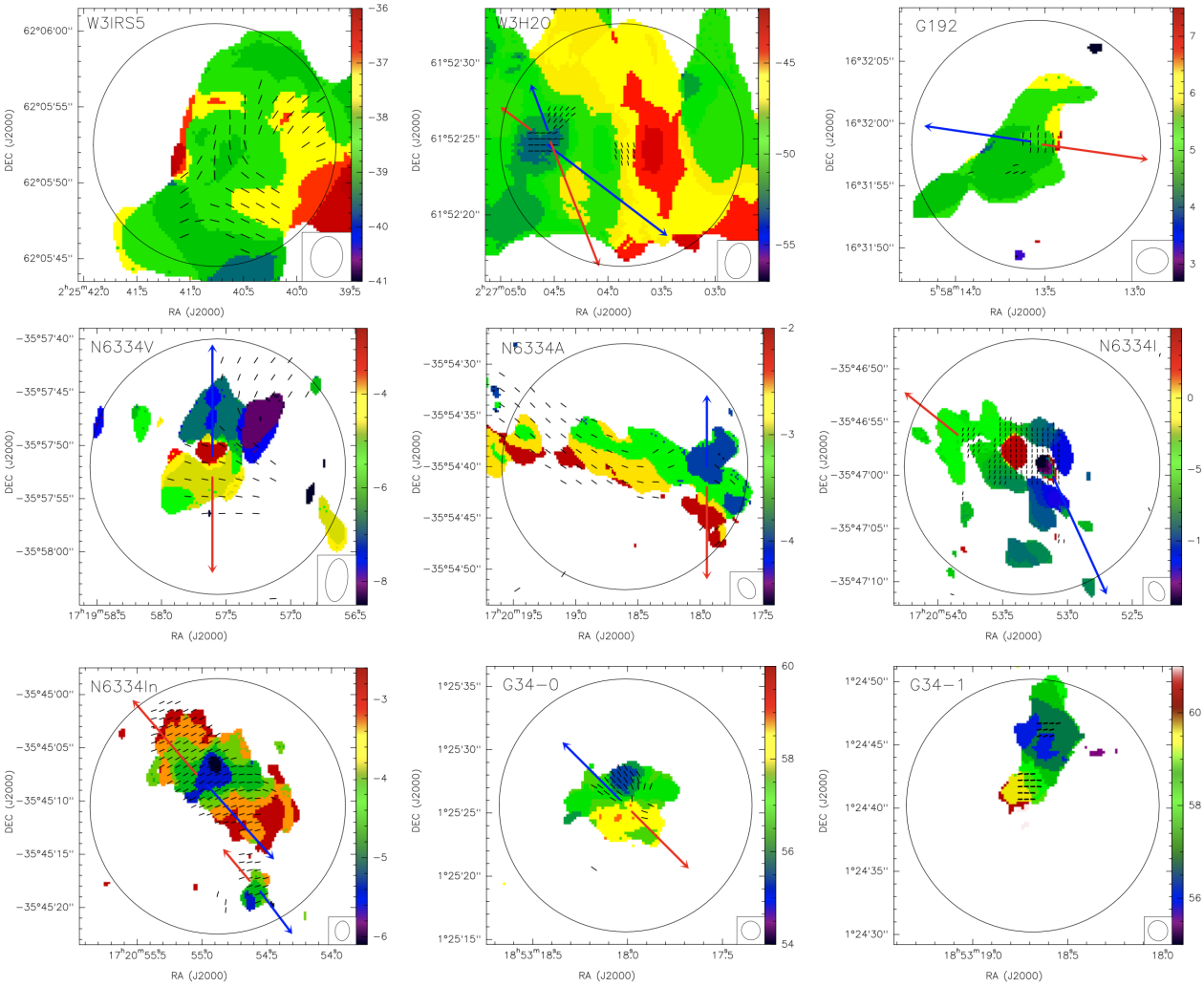

FIG. 14A.— First-order moments for $H^{13}CO^+$ (4–3) data with the magnetic field segments (black) overplotted. Red and blue arrows indicate the approximate orientations of the redshifted and blueshifted outflow emission according to Zapata et al. (2011), and Zhang et al. (2014). The synthesized beam is shown in the bottom-right corner. The circle corresponds to the field of view of 0.15 pc of diameter used in this work to assess the magnetic field strength. Wedge units are km s^{-1}.

COMPARISON OF SMA AND SINGLE-DISH DENSITIES

In Section 4.1, the density structure for each massive dense core was inferred using data from single-dish telescopes, mainly the James Clerk Maxwell Telescope (with main beams of 19.5″ at 850 μm and 11.0″ at 450 μm) and the IRAM 30m telescope (with a main beam of 11.0″ at 1.2 mm). From this model, the average density within 0.15 pc was derived. In order to asses if the different spatial filtering of the single-dish telescopes and the SMA is affecting our determination of the density and the magnetic field strength, we compare here how the inferred densities in Section 4.1 compare to the density inferred using the SMA data. The average density (within 0.15 pc of diameter) was estimated using the SMA continuum flux densities, including all the configurations available as for the case of the $H^{13}CO^+$ and PA data. This includes in many cases the subcompact configuration and in all cases the compact configuration of the SMA. These configurations allow to recover angular scales as large as 30″ and 14″, respectively (following the appendix of Palau et al. 2010). Therefore, using these SMA data we are sensitive to scales comparable to the scales of the single-dish telescopes. To infer the masses and densities from the SMA data, we measured the flux density within the region of 0.15 pc of diameter, and assumed the average temperature within the same diameter inferred from our modeling (given in Table 3), as well as the opacity law of Ossenkopf & Henning (1994, grains covered by thin ice mantles at 10^6 cm^{-3}, 0.0175 cm^2 per gram of gas and dust at 870 μm). Fig. 16 presents the relation between the SMA average density (within 0.15 pc of diameter) vs the average density inferred using the modeling of the single-dish data presented in Section 4.1. As can be seen from the figure, the amount of mass filtered out by the SMA is small, of only $\sim$ 25% of the mass inferred from the modeling of the single-dish data presented in Section 4.1.

COMPARISON OF MAGNETIC FIELD STRENGTH INFERRED IN THIS WORK AND THE MAGNETIC FIELD STRENGTH IN OTHER WORKS OF THE LITERATURE

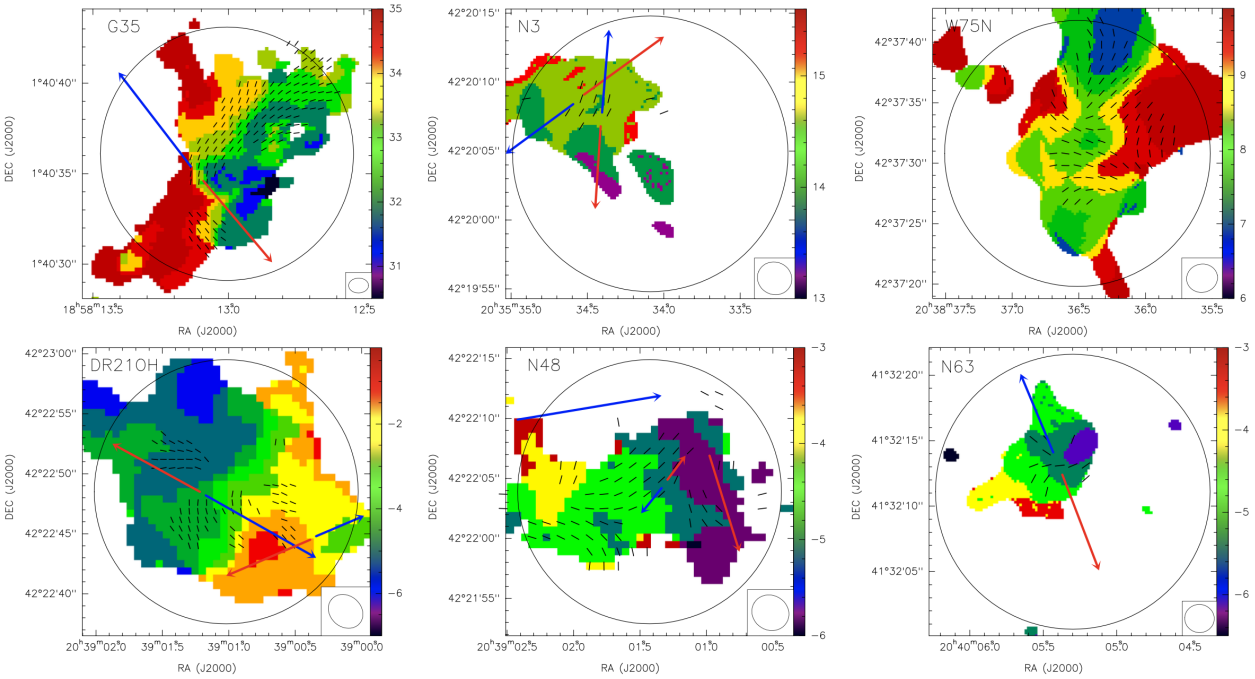

FIG. 14B.— First-order moments for $H^{13}CO^+$ (4–3) data with the magnetic field segments (black) overplotted. Red and blue arrows indicate the approximate orientations of the redshifted and blueshifted outflow emission according to Duarte-Cabral et al. (2013, 2014), Girart et al. (2013), and Zhang et al. (2014). The synthesized beam is shown in the bottom-right corner. The circle corresponds to the field of view of 0.15 pc of diameter used in this work to assess the magnetic field strength. Wedge units are km s^{-1}.

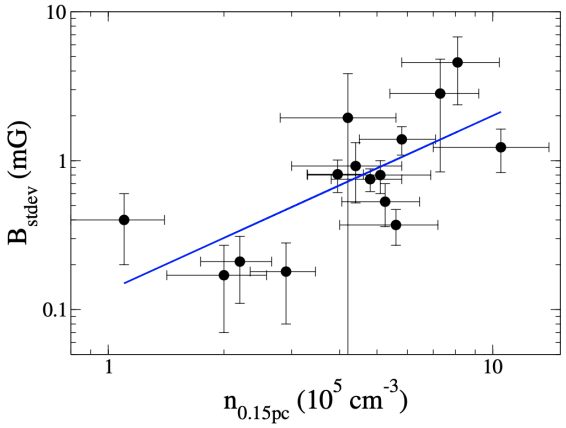

FIG. 15.— Magnetic field strength vs density averaged within 0.15 pc. The blue line corresponds to a linear fit in the log-log scale with a slope of 1.2.

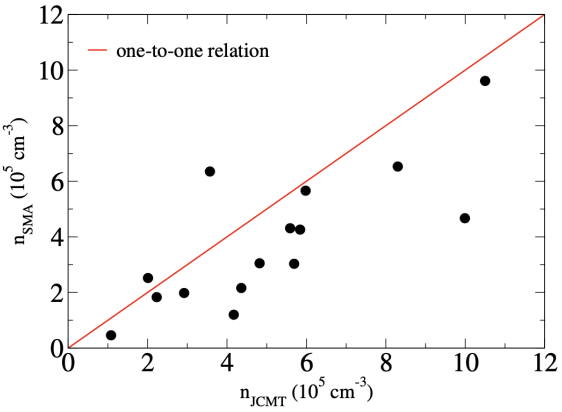

FIG. 16.— Plot of the SMA average density (within 0.15 pc of diameter) vs the average density inferred using the modeling of the single-dish data presented in Section 4.1.

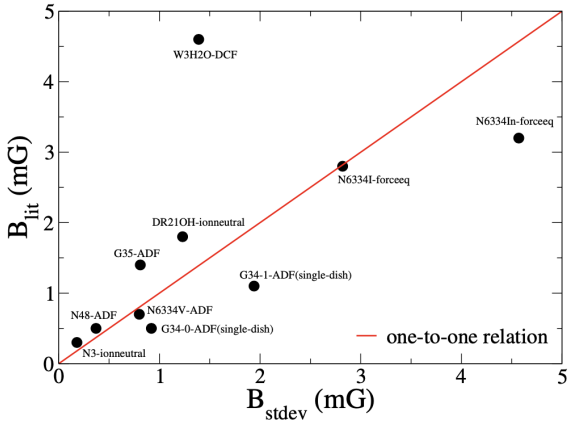

FIG. 17.— Comparison of the magnetic field determined in the literature and the magnetic field determined in this work, $B_{\rm stdev}$. The red line corresponds to the one-to-one relation to guide the eye. Next to the name of each source, there is a short-name for the method used to determine the magnetic field strength. See Table 4 for further details.